Low-rank magnetic resonance fingerprinting

Gal Mazor[a)] and Lior Weizman
Department of Electrical Engineering, Technion - Israel Institute of Technology, Haifa, Israel

Assaf Tal
Department of Chemical Physics, Weizmann Institute of Science, Rehovot, Israel

Yonina C. Eldar
Department of Electrical Engineering, Technion - Israel Institute of Technology, Haifa, Israel

Purpose: Magnetic resonance fingerprinting (MRF) is a relatively new approach that provides quantitative MRI measures using randomized acquisition. Extraction of physical quantitative tissue parameters is performed offline, without the need of patient presence, based on acquisition with varying parameters and a dictionary generated according to the Bloch equation simulations. MRF uses hundreds of radio frequency (RF) excitation pulses for acquisition, and therefore, a high undersampling ratio in the sampling domain (k-space) is required for reasonable scanning time. This undersampling causes spatial artifacts that hamper the ability to accurately estimate the tissue's quantitative values. In this work, we introduce a new approach for quantitative MRI using MRF, called magnetic resonance fingerprinting with low rank (FLOR).

Methods: We exploit the low-rank property of the concatenated temporal imaging contrasts, on top of the fact that the MRF signal is sparsely represented in the generated dictionary domain. We present an iterative recovery scheme that consists of a gradient step followed by a low-rank projection using the singular value decomposition.

Results: Experimental results consist of retrospective sampling that allows comparison to a well defined reference, and prospective sampling that shows the performance of FLOR for a real-data sampling scenario. Both experiments demonstrate improved parameter accuracy compared to other compressed-sensing and low-rank based methods for MRF at 5% and 9% sampling ratios for the retrospective and prospective experiments, respectively.

Conclusions: We have shown through retrospective and prospective experiments that by exploiting the low-rank nature of the MRF signal, FLOR recovers the MRF temporal undersampled images and provides more accurate parameter maps compared to previous iterative approaches. © *2018 American Association of Physicists in Medicine* [https://doi.org/10.1002/mp.13078]

1. INTRODUCTION

Quantitative magnetic resonance imaging (QMRI) is widely used to measure tissue's intrinsic spin parameters such as the spin-lattice magnetic relaxation time (T1) and the spin-spin magnetic relaxation time (T2).[1] Since tissue relaxation times vary in disease, QMRI enables the diagnosis of different pathologies, including multiple sclerosis (MS), Alzheimer, Parkinson, epilepsy, and cancer.[2–7] In addition, the knowledge of tissue relaxation times allows generation of many clinical MR imaging contrasts (such as FLAIR and STIR) offline, and saves a significant amount of scanning time.

Despite the advantages of QMRI, clinical MRI today mainly consists of weighted images. Values in weighted MR imaging are given in arbitrary units, since the signal strength is influenced by both intrinsic parameters (such as temperature, relaxation times and concentration of hydrogen atoms) and nonintrinsic ones. Nonintrinsic parameters include transmit and receive coils sensitivities, patient position in the scanner, and vendor-based scanner specific parameters.

Weighted MRI images therefore lack quantitative information and as a result, different materials may exhibit similar or identical gray level values. In addition, weighted MRI contrast values vary between different follow-up scans of the same patient. This fact may impair disease monitoring, if based solely on those images. To date, weighted MRI scans are more common than QMRI in the clinic, due to the extremely long times often associated with QMRI using conventional techniques.[8–10]

A plethora of methods have been proposed for QMRI. Earlier approaches are based on a series of spin echo (SE) or inversion recovery (IR) images with varying repetition times (TR) and echo times (TE) to evaluate each magnetic parameter (T1 or T2) separately. After acquisition, the curve of intensities for each pixel is matched to the expected magnetic signal, representing the appropriate magnetic tissue parameters.[8] Accelerated methods for QMRI consist of multiple-flip-angle methods,[11,12] the popular driven equilibrium single pulse observation of T1 (DESPOT1)[9] or T2 (DESPOT2)[10] and the IR TrueFISP for simultaneous recovery of T1 and T2

quantitative maps.[1,13] These techniques do not require long waiting times between excitations to reach an equilibrium state, and therefore are significantly faster. Later works shortened the acquisition time required by those methods by undersampling the data in both spatial and temporal domains.[14–18] However, obtaining accurate and high resolution QMRI in a reasonable clinical scanning time is still very challenging.

An approach for QMRI called magnetic resonance fingerprinting (MRF) has drawn increased attention in the last few years.[19] MRF uses pseudorandomized acquisitions to generate many different imaging contrasts, acquired at a high undersampling ratio. It exploits the different acquisition parameters over time to produce a temporal signature, a "fingerprint," for each material under investigation. By matching this unique signature to a pregenerated set of simulated patterns, the quantitative parameters can be extracted off-line. This approach saves valuable scan time compared to previous methods for accelerated QMRI, demonstrating promising efficient and reliable results.

MRF utilizes the fact that each tissue responds differently to a given quasi-random pulse sequence. By varying the acquisition parameters [e.g., repetition time (TR), echo time (TE), and radio frequency flip angle (FA)], unique signals are generated from different tissues. After acquisition, a pattern recognition algorithm is used to match the acquired signal from each voxel to an entry from a dictionary of possible tissue candidates. The dictionary entries are created by simulating the tissue's response to the sequence for a range of T1 and T2 parameter values, using the Bloch equations. The resulting dictionary contains the temporal signatures of

various simulated materials, given the pseudorandom pulse sequence. The quantitative parameters, such as the tissue's T1 and T2 relaxation times, can be retrieved from the data by matching the signature acquired to the most correlated entry in the dictionary.

In MRI, data are acquired in the Fourier domain of the spatial image (a.k.a. k-space). The acquisition time of a high-resolution, single-contrast three-dimensional (3D) MRI lasts a substantial amount of time. Since MRF is based on rapid acquisition of hundreds of different contrasts, severe undersampling is performed in k-space to obtain the temporal resolution required for MRF. Figure 1 demonstrates the effect of fully sampled vs undersampled data, acquired with spiral trajectories and recovered using the inverse nonuniform fast Fourier transform (NUFFT).[20] It can be seen that the undersampled data is blurred and introduces aliasing artifacts. Figure 2 illustrates the noise and undersampling artifacts of a representative brain voxel intensity as function of time, where the data is acquired with an MRF sequence based on fast imaging with steady-state precession (FISP).[21] Clearly, undersampling also introduces a substantial level of noise in the time domain. In addition, MRF uses a dictionary with discrete values, while QMRI values are continuous. This leads to quantization error, depending on the values represented in the dictionary.

While in the original MRF paper[19] these imaging artifacts are not handled explicitly, recent works have implemented advanced reconstruction techniques to overcome undersampling artifacts. Approaches based on exploiting the sparsity of the signal in some transform domain in a compressed sensing (CS)[22,23] framework are examined by Davies et al.[24] and
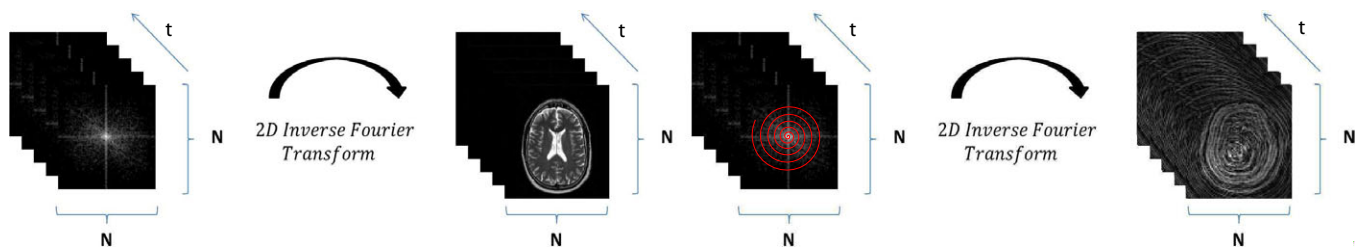

FIG. 1.   Illustration of fully sampled (left) vs spiral trajectory undersampled (right) k-spaces and their corresponding reconstructed images using direct inverse Fourier transform. In MRF, we acquire many undersampled images over time. When reconstructed by NUFFT, the undersampled data is blurred and contains aliasing artifacts. [Color figure can be viewed at wileyonlinelibrary.com]
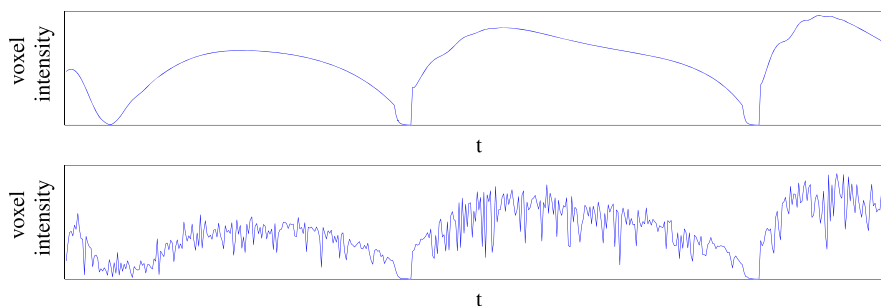

FIG. 2.   Illustration of a single brain voxel's temporal signature acquired with an MRF approach based on the FISP sequence. Fully sampled (top) vs noisy and undersampled (bottom) at 15% sampling ratio. [Color figure can be viewed at wileyonlinelibrary.com]

Wang et al.[25]. Zhao et al. [26] formulated MRF as a maximum likelihood (ML) problem, and developed an iterative reconstruction approach in order to estimate the magnetic parameters. While these techniques showed improved results compared to the original MRF method, they do not exploit the temporal similarity between adjacent time-points, which is intrinsic to the dynamic acquisition used in MRF.

A common approach to exploit redundancy exists in dynamic MRI that is based on modeling the acquired data as low-rank.[27,28] This modeling was successfully applied for various dynamic MRI applications, such as cardiac imaging[29,30] and functional MRI.[31] In the context of MRF, early works use low-rank MRF to compress the dictionary for faster reconstruction.[32,33] This saves reconstruction time, but does not necessarily improve the quality of the reconstructed maps or the acquisition time. The first introduction of a subspace constrained low-rank approach for improved reconstruction in MRF was proposed by Zhao et al.[34,35] Following these works, we suggested our variant for a subspace constrained low-rank approach.[36] Liao et al. presented an extension of these ideas by adding a sparse term to the low-rank-based reconstruction[37] (a.k.a robust PCA[38]). Doneva et al.[39,40] assume that the k-t data matrix has a low-rank, and presented an approach based on matrix completion in the k-space domain. As opposed to conventional low-rank based approaches that estimate the unknown rank from undersampled data, in their approach the data subspace is estimated from a small subset of fully sampled k-space data (a.k.a. calibration data). While innovative, their implementation requires a unique MRF acquisition to ensure that this calibration data is acquired properly. Therefore, it may not be applicable for reconstruction of previously acquired MRF data. Recently, a few approaches that utilize prior knowledge of the dictionary together with a low-rank constraint have been published. Zhao et al.[41] presented an efficient algorithm that performs a singular value decomposition (SVD) on the dictionary and embeds the right singular vectors into the solution, to obtain better estimation of the temporal signatures. A similar approach was presented by Assländer et al.[42], who embed the left singular vectors. These methods show that exploiting the redundancy via a low-rank based solution improves the results compared to a sparsity approach. However, the obtained reconstructed maps still suffer from quantization error, due to the nature of a matched-filter-based solution that matches a single dictionary atom to a single pixel. In addition, most of these techniques are based on a fixed rank, set in advance, which may be difficult to determine in advance.

In this paper, we extend our initial idea presented in our conference paper[36] and enforce a low-rank constraint in the image domain together with constraining the solution to the dictionary subspace. In particular, we exploit the low-rank property of the temporal MRF domain, via an iterative scheme that consists of a gradient step followed by a projection onto the subspace spanned by the dictionary elements in order to constrain the structure of the tissue behavior simulated in the dictionary. The estimated images are then decomposed using SVD and the singular values are soft-thresholded to reduce the nuclear norm in every step. Our approach, called magnetic resonance fingerprinting with low rank constraint (FLOR), incorporates three main advantages that were only partially introduced in previous work:

- FLOR formulates the recovery problem of finding the temporal images as a convex problem. The solution is then rigorously developed based on the incremental subgradient proximal method.[43] This technique is known to converge to the global minimum, regardless of the initial starting point.
- FLOR is based on nuclear-norm minimization, and does not require fixing the rank in advance. This leads to a solution that adapts the rank according to the nature of the specific dataset.
- The subspace constraint in FLOR is not limited to dictionary items, but rather allows a solution that is spanned by the dictionary. This enables better reconstruction of the temporal imaging contrasts. It also allows generation of quantitative parameters that do not necessarily exist in the simulated dictionary, thereby reducing the quantization error of the resulting maps.

While there are previous publications that introduce one or two of the advantages pointed above (e.g., Zhao et al.[41] describes a subspace constraint that is not limited to the dictionary items), our work incorporates all of them together in a convenient optimization framework.

Our reconstruction results are based on sampling with variable density spiral trajectories, using 5% and 9% sampling ratios, for retrospective and prospective experiments, respectively. We compare our results to the methods developed by Davies et al.[24] and Zhao,[34] and show that FLOR provides quantitative parameter maps with higher accuracy or correspondence to literature compared to those techniques.

This paper is organized as follows. Section 2 describes the MRF problem and provides a review of common reconstruction methods, followed by our low-rank based approach. Section 3 compares our results to previous MRF algorithms, using retrospective and prospective undersampled MRF data of a human subject. Sections 4 and 5 include a discussion on the experimental results, followed by conclusions.

2. MATERIALS AND METHOD

2.A. Problem formulation

MRF data consists of multiple frames, acquired in the image's conjugate Fourier domain (a.k.a k-space), where each frame results from different acquisition parameters. We stack the measurements into a $Q \times L$ matrix $\mathbf{Y}$, where L is the number of frames and Q is the number of k-space samples in each frame. Every column in $\mathbf{Y}$ is an undersampled Fourier transform of an image frame, $\mathbf{X}_{:,i}$:

$$\mathbf{Y} = [F_u\{\mathbf{X}_{:,1}\}, \ldots, F_u\{\mathbf{X}_{:,L}\}] + \mathbf{H} \tag{1}$$

where $F_u\{\cdot\}$ denotes an undersampled two-dimensional (2D) Fourier transform and $\mathbf{H}$ denotes a zero mean complex Gaussian noise. The row $\mathbf{X}_{j,:}$ represents the temporal signature of a single pixel (assumed to correspond to a single tissue). The signature depends on the tissue's relaxation times, T1 and T2, and its proton density (PD), grouped as a row vector:

$$\mathbf{\Theta}_1^j = [T1^j, T2^j, PD^j], \quad 1 \le j \le N. \tag{2}$$

Each column, $\mathbf{X}_{:,i}$ represents a response image acquired at a single time point with different acquisition parameters, stacked as a column vector:

$$\mathbf{\Theta}_2^i = [TR^i, TE^i, FA^i]^T, \quad 1 \le i \le L \tag{3}$$

where TR and TE are the repetition time and time to echo and FA represents the flip angle of the RF pulse. Therefore, $\mathbf{X}_{j,:} = f(\mathbf{\Theta}_1^j, \mathbf{\Theta}_2)$, where $f\{\cdot\}$ represents the Bloch equations. Note that we omit the off-resonance parameter (which appeared in $\mathbf{\Theta}_1$ in the original MRF paper[19]), since the sequence used in our retrospective experiments is derived from the FISP sequence, which is insensitive to off resonance effects.[21]

The goal in MRF is to recover, from the measurements $\mathbf{Y}$, the imaging contrasts $\mathbf{X}$ and the underlying quantitative parameters of each pixel defined in Eq. (2), under the assumptions that every pixel in the image contains a single type of tissue and that $\mathbf{\Theta}_2$ is known.

Recovery is performed by defining a dictionary that consists of simulating the signal generated from M tissues using the Bloch equations (represented as M different combinations of T1 and T2 relaxation times), when the length-L acquisition sequence defined in Eq. (3) is used. As a result, we obtain a dictionary $\mathbf{D}$ of dimensions $M \times L$ ($M > L$ as the number of simulated tissues is greater than the sequence length). The PD is not simulated in the dictionary, as it is the gain used to match the Bloch simulation performed on a single spin to the signal obtained from a pixel containing multiple spins. It can be easily determined after the T1 and T2 maps are known. After successful recovery of $\mathbf{X}$, each row in $\mathbf{X}$ is matched to a single row in the dictionary, and T1 and T2 are estimated as those used to generate the matched dictionary row. Every dictionary signature has its own unique T1 and T2 values stored in a lookup table (LUT), represented as the matrix $\mathbf{LUT}$ of dimensions $M \times 2$.

2.B. Previous methods

The approach suggested in the original MRF paper[19] is described in Algorithm 1, and uses matched filtering to match dictionary items to the acquired data. In the algorithm, $F^H\{\cdot\}$ is the 2D inverse NUFFT operator. The parameters k_j are the matching dictionary indices, j is a spatial index and i is the temporal index, representing the ith frame in the acquisition. The parameter maps are extracted from $\mathbf{LUT}$, which holds the values of T1 and T2 for each k_j. This approach does not incorporate sparse based reconstruction, which has been proven to be very successful in MRI applications based on undersampled data.[44–46]

Davies et al.[24] suggested a method incorporating sparsity of the data in the dictionary domain (i.e., each pixel is represented by at most one dictionary item), referred to as the BLoch response recovery via Iterative Projection (BLIP) algorithm. This approach is based on the projected Landweber algorithm (PLA), which is an extension of the popular iterative hard thresholding method. BLIP (described here as Algorithm 2) consists of iterating between two main steps: A gradient step that enforces consistency with the measurements, and a projection that matches each row of $\mathbf{X}$ to a single dictionary atom.

Algorithm 1. Original MRF algorithm

Input:
A set of k-space samples: $\mathbf{Y}$
A pre simulated dictionary: $\mathbf{D}$
An appropriate look up table: $\mathbf{LUT}$
Output:
Magnetic parameter maps: $\widehat{T}_1, \widehat{T}_2, \widehat{PD}$
Compute for every i and j:

$$\widehat{\mathbf{X}}_{:,i} = F^H\{\mathbf{Y}_{:,i}\}$$

$$\widehat{k}_j = \arg\max_k \frac{|\langle D_k, \widehat{\mathbf{X}}_{j,:}\rangle|}{||D_k||_2}$$

$$\widehat{T}_1^j, \widehat{T}_2^j = \mathbf{LUT}(\widehat{k}_j)$$

$$\widehat{PD}^j = \max\left\{\frac{\text{real}\langle D_{\widehat{k}_j}, \widehat{\mathbf{X}}_{j,:}\rangle}{||D_{\widehat{k}_j}||_2^2}, 0\right\}$$

Algorithm 2. BLIP

Input:
A set of k-space samples: $\mathbf{Y}$
A pre simulated dictionary: $\mathbf{D}$
An appropriate look up table: $\mathbf{LUT}$
Output:
Magnetic parameter maps: $\widehat{T}_1, \widehat{T}_2, \widehat{PD}$
Initialization: $\mu, \widehat{\mathbf{X}}^0 = 0$
Iterate until convergence:

- Gradient step for every i:
$$\widehat{\mathbf{Z}}_{:,i}^{n+1} = \widehat{\mathbf{X}}_{:,i}^n - \mu F^H\{F_u\{\widehat{\mathbf{X}}_{:,i}^n\} - \mathbf{Y}_{:,i}\}$$

- Project onto the dictionary subspace for every j:
$$\widehat{k}_j = \arg\max_k \frac{|\langle D_k, \widehat{\mathbf{z}}_{j,:}\rangle|}{||D_k||_2}$$

$$\widehat{PD}^j = \max\left\{\frac{\text{real}\langle D_{\widehat{k}_j}, \widehat{\mathbf{z}}_{j,:}\rangle}{||D_{\widehat{k}_j}||_2^2}, 0\right\}$$

$$\widehat{\mathbf{X}}_{j,:}^{n+1} = \widehat{PD}^j \mathbf{D}_{\widehat{k}_j}$$

Restore maps for every j: $\widehat{PD}^j, \widehat{T}_1^j, \widehat{T}_2^j = \mathbf{LUT}(\widehat{k}_j)$
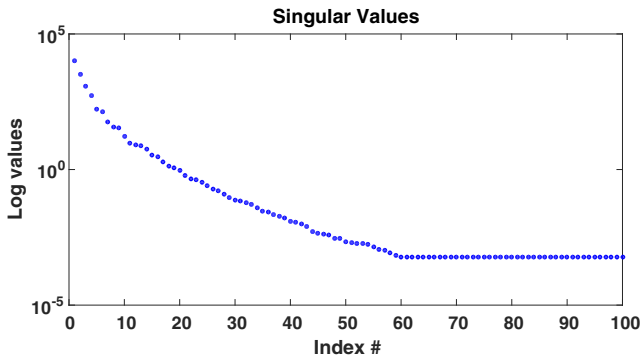
Singular Values

FIG. 3. Singular values of FISP MRF sequence images in descending order. Singular values #1–#100 are shown, out of a total 500 singular values, presenting an effectively low-rank matrix. [Color figure can be viewed at wileyonlinelibrary.com]

BLIP and a few other works that are based on it[25] do not incorporate the temporal similarity across time points, which is a fundamental characteristic of the MRF sequence. In addition, there is a high degree of similarity across signatures in **D**. As a result, the space-time matrix **X** is typically a low-rank matrix.

Low-rank based modeling for dynamic MRI in general[30,31,47,48] and MRF in particular[32–42] has been proposed in the past. To demonstrate the low-rank property of **X**, we used T1, T2, and PD maps of size 128×128 (acquired using DESPOT[49]) as an input to a simulation of a FISP sequence[21] (simulated using the extended phase graph (EPG)).[50] The acquisition length in this experiment was $L = 500$ TRs. In addition, we used random TR and FA values that have been used in previous publications in the field of MRF.[19,21] Note that the general assumption of **X** being a low-rank matrix holds as long as temporal similarity exist between timeframes in **X**, and multiple voxels in the image belong to a single tissue, regardless of the specific acquisition parameters. Figure 3 shows the singular values of **X**. It can be seen that **X** is indeed low-rank, as most of the data is represented in top 10% highest singular values, out of a total number of 500 singular values.

This low-rank property of **X** can be exploited for improved reconstruction using the following optimization problem:

$$\underset{\mathbf{X},\mathbf{R}}{\text{minimize}} \quad \frac{1}{2}\underset{i}{\Sigma}\left\|\mathbf{Y}_{:,i} - F_u\{\mathbf{X}_{:,i}\}\right\|_2^2$$
$$\text{subject to } \text{rank}(\mathbf{X}) \leq r$$
$$\mathbf{X} = \mathbf{R}_1\mathbf{D} \qquad (4)$$

where $\mathbf{R}_1$ is a matrix that matches each pixel ($\mathbf{X}_{j,:}$) with the dictionary signatures. In many previous implementations of low-rank for MRF, a matching of a single dictionary atom to a single pixel is enforced, which means that the rows of $\mathbf{R}_1$ are one-sparse vectors. The parameter r is the rank of the matrix, and is usually defined as a fixed prechosen parameter. Typically r is not known in advance and determining it upfront arise difficulty and may add error to the reconstruction scheme.

Algorithm 3. Model Based Iterative Reconstruction MRF (MBIR-MRF)

Input:
A set of k-space samples: **Y**
A pre simulated dictionary: **D**
An appropriate look up table: **LUT**
Output:
Magnetic parameter maps: $\widehat{T}_1, \widehat{T}_2, \widehat{PD}$
Initialization: $\lambda, p < 1, \eta_1, \eta_2, \mathbf{R}^0, \mathbf{Z}^0, \mathbf{Q}^0, \mathbf{W}^0 = 0, \widehat{\mathbf{X}}_{:,i}^0 = F^H\{\mathbf{Y}_{:,i}\}$ for every i
Iterate until convergence:

- Find 1-sparse **R** as follows:

$$\widehat{k}_j = \underset{k}{\arg\max} \frac{\left|\left\langle D_{k,}, \left(\widehat{\mathbf{X}}^n + \frac{1}{\eta_1}\mathbf{Q}^n\right)_{j,:}\right\rangle\right|}{\|D_k\|_2}$$

$$\mathbf{R}_{j,\widehat{k}_j}^{n+1} = \frac{\left\langle D_{\widehat{k}_j}, \left(\widehat{\mathbf{X}}^n + \frac{1}{\eta_1}\mathbf{Q}^n\right)_{j,:}\right\rangle}{\|D_{\widehat{k}_j}\|_2^2}$$

- Update $\mathbf{Z}^{n+1}$ by soft-thresholding the singular values:

$$[\mathbf{U}, \mathbf{S}, \mathbf{V}] = \text{svd}\left(\widehat{\mathbf{X}}^n + \frac{1}{\eta_2}\mathbf{W}^n\right)$$

Soft-threshold the non-zero singular values $\{\sigma\}_j$ of **S** with parameter $\lambda\sigma_j^{p-1}$:

$$\sigma_j = \begin{cases} \sigma_j - \lambda\sigma_j^{p-1} & \sigma_j > \lambda\sigma_j^{p-1} \\ 0 & \text{otherwise} \end{cases}$$

$$\widehat{\mathbf{Z}}^{n+1} = \mathbf{U}\mathbf{S}\mathbf{V}^H$$

- Update **Q** and **W**

$$\mathbf{Q}^{n+1} = \mathbf{Q}^n + \eta_1\left(\mathbf{X}^n - \mathbf{R}^{n+1}\mathbf{D}\right)$$
$$\mathbf{W}^{n+1} = \mathbf{W}^n + \eta_2\left(\mathbf{X}^n - \mathbf{Z}^{n+1}\right)$$

- Update $\mathbf{X}^{n+1}$ by solving the following minimization problem:

$$\underset{\mathbf{X}}{\text{minimize}} \quad \frac{1}{2}\underset{i}{\Sigma}\|\mathbf{Y}_{:,i} - F_u\{\mathbf{X}_{:,i}\}\|_2^2 + \eta_1\left\|\mathbf{Q}^{n+1} - \mathbf{X} + \mathbf{R}^{n+1}\mathbf{D}\right\|_F^2$$
$$+ \eta_2\left\|\mathbf{W}^{n+1} - \mathbf{X} + \mathbf{Z}^{n+1}\right\|_F^2$$

Restore maps for every j:
$$\widehat{PD}^j = \max\left\{\mathbf{R}_{j,\widehat{k}_j}^{n+1}, 0\right\}, \widehat{T}_1^j, \widehat{T}_2^j = \mathbf{LUT}(\widehat{k}_j)$$

Zhao et al.[34] suggested an approximation for problem (2), using an ADMM formulation[51] as follows:

$$\mathbf{X}^{n+1}, \mathbf{R}_1^{n+1}, \mathbf{Z}^{n+1} = \underset{\mathbf{X},\mathbf{R}_1,\mathbf{Z}}{\arg\min} \frac{1}{2}\underset{i}{\Sigma}\left\|\mathbf{Y}_{:,i} - F_u\{\mathbf{X}_{:,i}\}\right\|_2^2$$
$$+ \lambda\psi(\mathbf{Z}) + \eta_1\left\|\mathbf{Q}^n - \mathbf{X} + \mathbf{R}_1\mathbf{D}\right\|_F^2$$
$$+ \eta_2\left\|\mathbf{W}^n - \mathbf{X} + \mathbf{Z}\right\|_F^2$$
$$\mathbf{Q}^{n+1} = \mathbf{Q}^n + \eta_1\left(\mathbf{X}^{n+1} - \mathbf{R}_1^{n+1}\mathbf{D}\right)$$
$$\mathbf{W}^{n+1} = \mathbf{W}^n + \eta_2\left(\mathbf{X}^{n+1} - \mathbf{Z}^{n+1}\right)$$
$$(5)$$

where the low-rank constraint is applied via the function $\psi(\mathbf{Z})$, defined as the P norm ($P < 1$) of the singular values of **Z** to the power of P. The matrices **Q** and **W** are the Lagrange multipliers. The method, coined as model-based iterative reconstruction MRF (MBIR-MRF),[34] is described in Algorithm 3.

2.C. Proposed method

The constraint presented in previous approaches[34] on $\mathbf{R}_1$ to have one sparse rows that contain the corresponding PD values for each row of **X**, is justified by the assumption that only a single dictionary item should match an acquired signature. However, in practice, we found that superior results (in terms of spatial resolution and correspondence to ground truth) are obtained by relaxing this constraint, and allowing **X** to be comprised of multiple

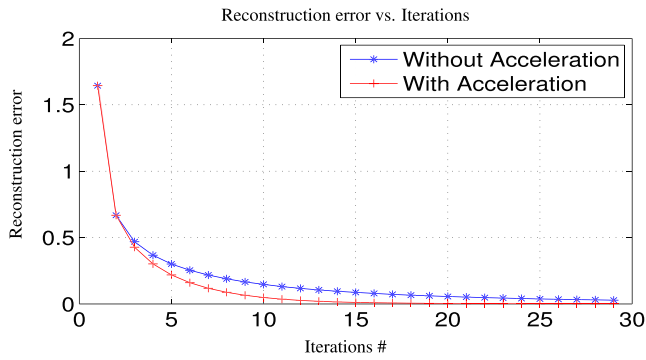Reconstruction error vs. Iterations

FIG. 4. Comparison between the convergence of accelerated (plus sign) and standard (asterisk) FLOR. [Color figure can be viewed at wileyonlinelibrary.com]

dictionary elements at each step of the optimization algorithm, where at the final stage each voxel is matched to a single tissue. This allows for nonsimulated signatures to be described by a linear combination of simulated ones. In addition, the relaxation enables formulating the problem as a convex problem, and saves the pattern recognition search time during reconstruction. The matching between **X** and the dictionary is performed only at the final stage, after **X** is fully recovered by using a matched filter (MF), in order to extract the parameter maps. For brevity, we write the constraint **X** = **RD** as **X** $\in \mathbb{D}$ where $\mathbb{D} = \{\mathbf{X} : \mathcal{N}(\mathbf{X}) \supseteq \mathcal{N}(\mathbf{D})\}$, and consider the following regularized form:

$$\underset{\mathbf{X} \in \mathbb{D}}{\text{minimize}} \frac{1}{2} \underset{i}{\Sigma} \left\| \mathbf{Y}_{:,i} - F_u\{\mathbf{X}_{:,i}\} \right\|_2^2 + \lambda \text{rank}(\mathbf{X}) \qquad (6)$$

for some fixed regularization parameter λ.

Problem (6) is not convex due to the rank constraint. We therefore relax this constraint by replacing the rank of **X** with the nuclear norm $\|\mathbf{X}\|_*$, defined as the sum of the singular values of **X**.[52] This results in the relaxed problem:

$$\underset{\mathbf{X} \in \mathbb{D}}{\text{minimize}} \frac{1}{2} \underset{i}{\Sigma} \left\| \mathbf{Y}_{:,i} - F_u\{\mathbf{X}_{:,i}\} \right\|_2^2 + \lambda \|\mathbf{X}\|_*. \qquad (7)$$

In order to solve (7), we use the incremental subgradient proximal method[53] described in Appendix A.

Due to the convex modeling of the problem, we also introduce an improvement that significantly reduces convergence time. The improvement uses the acceleration approach suggested by Nesterov[54] for minimizing a smooth convex function, and its extension for nonsmooth composite functions of Beck and Teboulle.[55,56] Our final algorithm is detailed in Algorithm 4 and referred to as FLOR, where the parameter λ is chosen experimentally. Note that by setting $\lambda = 0$, enforcing **R** to have one-sparse rows and eliminating the acceleration step, FLOR reduces to BLIP.[24]

Figure 4 shows the reconstruction error of FLOR as the number of iterations varies with and without the

acceleration step. Note that the CPU time of both algorithms is similar.

Algorithm 4. FLOR - MRF with LOw Rank

Input:
A set of k-space samples: **Y**
A pre simulated dictionary: **D**
An appropriate look up table: **LUT**
Output:
Magnetic parameter maps: $\widehat{T}_1, \widehat{T}_2, \widehat{PD}$
Initialization: $\mu, \lambda, t_0 = 1, \widehat{\mathbf{X}}^0 = \mathbf{0}, \mathbf{P} = \mathbf{D}^\dagger \mathbf{D}$
Iterate until convergence:

• Gradient step for every i:

$$\widehat{\mathbf{Z}}_{:,i}^{n+1} = \widehat{\mathbf{X}}_{:,i}^n - \mu F^H \{F_u\{\widehat{\mathbf{X}}_{:,i}^n\} - \mathbf{Y}_{:,i}\}$$

• Project onto the dictionary subspace and soft-threshold the singular values:

$$[\mathbf{U}, \mathbf{S}, \mathbf{V}] = \text{svd}\left(\widehat{\mathbf{Z}}^{n+1}\mathbf{P}\right)$$

Soft-threshold the non-zero singular values $\{\sigma\}_j$ of **S** with parameter $\lambda\mu$:

$$\sigma_j = \begin{cases} \sigma_j - \lambda\mu & \sigma_j > \lambda\mu \\ 0 & \text{otherwise} \end{cases}$$

$$\widehat{\mathbf{M}}^{n+1} = \mathbf{U}\mathbf{S}\mathbf{V}^H$$

• Acceleration step:

$$t_{n+1} = \frac{1 + \sqrt{1 + 4t_n^2}}{2}$$

$$\widehat{\mathbf{X}}^{n+1} = \widehat{\mathbf{M}}^{n+1} + \frac{t_n - 1}{t_{n+1}}\left(\widehat{\mathbf{M}}^{n+1} - \widehat{\mathbf{M}}^n\right)$$

Restore maps for every j:

$$\widehat{k}_j = \arg\max_k \frac{|\langle D_k, \widehat{\mathbf{X}}_{j,:}\rangle|}{\|D_k\|_2}$$

$$\widehat{T}_1^j, \widehat{T}_2^j = \mathbf{LUT}(\widehat{k}_j)$$

$$\widehat{PD}^j = \max\left\{\frac{\text{real}\langle D_{\widehat{k}_j}, \widehat{\mathbf{X}}_{j,:}\rangle}{\|D_{\widehat{k}_j}\|_2^2}, 0\right\}$$

2.D. Possible extension

Conventional MRF algorithms use a MF for the magnetic parameter extraction. The MF operation introduces quantization error since map values are continuous, as opposed to discrete dictionary values. A possible extension of FLOR is to add elements to the dictionary by linear interpolation, in regions where a few candidates from the dictionary match a single signature from the data. We then select the dictionary signatures that exhibit a high correlation value (the ones above a certain threshold) and average their matching T1 and T2 values. An algorithm that incorporates this extension is given as Algorithm 5, where "Max(·)" indicates a function that finds the maximal element in a vector, and "Interpolate (·)" indicates linear interpolation of a vector. Note that this Algorithm is replaces the final stage of Algorithm 4 (the restoration of the maps which is implemented as a standard MF in Algorithm 4).

This improvement expands the possible solutions to include ones that do not exist in the dictionary, and therefore exhibits improved accuracy compared to the conventional matching. The major benefit from this extension is reduced quantization errors that arise from conventional MF used in MRF. This extension, coined FLOR II, is

examined in the first part of our experimental results in the next section.

Algorithm 5. FLOR II - (Extension to improve MF stage)

Input:
Estimated imaging contrasts : $\hat{\mathbf{X}}$
A pre simulated dictionary: $\mathbf{D}$
An appropriate look up table: **LUT**
Threshold for interpolated dictionary candidates inclusion: th_1

Output:
Magnetic parameter maps: $\widehat{T}_1, \widehat{T}_2, \widehat{PD}$

Repeat for every pixel in $\hat{\mathbf{X}}$ (j serves as a spatial index):

- Find MF score for every dictionary item:
  $s_m = \frac{|\langle D_m, \hat{\mathbf{X}}_{j,:}\rangle|}{||D_m||_2}$

- Interpolate both **LUT** and $\mathbf{s}$ to a finer T_1 and T_2 scale. Store interpolated results in $\mathbf{LUT}_I$ and $\mathbf{s}_I$:
  $\{\mathbf{LUT}_I, \mathbf{s}_I\} = \text{Interpolate}\{\mathbf{LUT}, \mathbf{s}\}$

- Find highest MF score in $\mathbf{s}_I$:
  $s_I^{\max} = \text{Max}(\mathbf{s}_I)$

- Find the indices of elements in $\mathbf{s}_I$ that are within th_1 of the maximal value:
  $\{l_q\}_{q=1}^Q = \{l : |s_I^l - s_I^{\max}| < th_1\}$

- Estimate T_1 and T_2 values as average values over the interpolated look up table ($\mathbf{LUT}_I$),
  for the selected elements:
  $\widehat{T}_1^j, \widehat{T}_2^j = \frac{1}{Q} \sum_{q=1}^{Q} \mathbf{LUT}_I(l_q)$

- Use Bloch simulation to estimate $\mathbf{d}_j$, the dictionary entry for $\widehat{T}_1^j, \widehat{T}_2^j$, and estimate proton density as:
  $\widehat{PD}^j = \max\left\{\frac{\text{real}\langle \mathbf{d}_j, \hat{\mathbf{X}}_{j,:}\rangle}{||\mathbf{d}_j||_2^2}, 0\right\}$

3. EXPERIMENTAL RESULTS

This section describes two MRI experiments that were carried out using brain scans of a healthy subject. The first experiment is based on well-known quantitative maps that were used, in a purely simulation environment to generate an MRF experiment with retrospectively sampled data. While this experiment is a simulation based on real quantitative maps, it allows accurate comparison of the results of the different algorithms using a well defined reference.

In the second experiment, we used prospective sampled real MRF data that was used to generate the results in Ma et al.[19] While this experiment lacks a gold standard for accurate error evaluation, it allows comparison between different algorithms in a realistic multicoil acquisition. To compare between different algorithms, for prospective sampling, where no ground truth is available, we examined the performance of the various algorithms as a function of the total number of excitations, where correspondence to values provided in literature for various brain tissues is used for validation. In both experiments, variable density spiral trajectories were used for sampling.

In the first experiment, forward and inverse nonuniform Fourier transforms were applied using SPURS, which is a fast approach published recently.[57] For the second experiment, we used the NUFFT package,[20] to adhere with the reconstruction results of the original MRF paper.[19] The reconstruction times for all methods examined is given in Table I. The long reconstruction times required for experiment 2 are mainly due to the fact that multicoil

TABLE I. Reconstruction times (in minutes).

Experiment #	BLIP	Method MBIR	FLOR
Experiment 1	19	56	23
Experiment 2	152	509	205

acquisition was used in that experiment, as opposed to experiment 1.

3.A. Experiment 1: Retrospective undersampling of simulated data

This experiment is based on simulating the acquisition of data with known quantitative parameters. The reference parameters maps were obtained by applying DESPOT1 and DESPOT2 methods on realistic brain scans. Those scans were acquired with a GE Signa 3T HDXT scanner. The procedures involving human subjects described in this experiment were approved by the Institutional Review Board of Tel-Aviv Sourasky Medical Center, Israel. We generated our reference data by acquisition of Fast Imaging Employing Steady-state Acquisition (FIESTA) and Spoiled Gradient Recalled Acquisition in Steady State (SPGR) images, at four different flip angles (3°, 5°, 12° and 20°), implementing the fast and well known DESPOT1 and DESPOT2[49] algorithms, after improvements as described in Liberman et al.[58], to generate T1,T2, and PD quantitative maps, each of size 128×128 pixels. While it is well known that the gold standard method for T1 measurement is the inversion recovery spin echo with varying TIs and for T2 measurement is the spin echo sequences with varying TEs, in this experiment, DESPOT was used as a reference thanks to its availability and its relatively fast acquisition time. The FISP pulse sequence has been applied for simulating acquisition of the reference, [FISP was simulated using extended phase graph (EPG)].[50] It was simulated with constant TE of 2 ms, random TR values in the range of 11.5–14.5 ms, and a sinusoidal variation of FA (RF pulses) in the range of 0–70 degrees.[21] The acquisition length in this experiment was $L = 500$ TRs.

To simulate noisy undersampled MRF samples, we added complex Gaussian zero-mean noise to the k-space data to obtain an SNR of 67 dB in the undersampled measurement domain. Data were then undersampled to acquire only 876 k-space samples in each TR with spiral trajectories. In particular, we used 24 variable density spirals with inner region size of 20 and FOV of 24. In every time frame, each spiral is shifted by 15 degrees. Figure 5 demonstrates the first spiral trajectory. We define the undersampling ratio by the number of the acquired samples in the k-space domain divided by the number of pixels in the generated image. This leads to an undersampling ratio of $\sim 5\%$ in this experiment. For comparison, the undersampling ratio of the original MRF paper[19] is $\sim 9\%$, since for each single spiral 1450 data points were acquired.

We generated the dictionary using Bloch equations, simulating T1 values of [100:20:2000,2300:300:5000] ms and T2 values of [20:5:100,1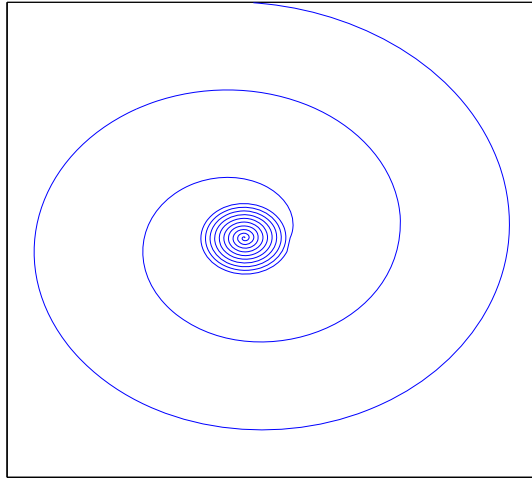10:10:200,300:200:1900] ms. This range covers the relaxation time values that can be found in a healthy brain scan.[59] The tuning parameters were experimentally set as $\mu = 1$ and $\lambda = 5$, after λ was tested in the range between 0 and 30. Data were fed as an input to BLIP, MBIR-MRF, and the improved FLOR algorithm (described as Algorithms 2, 3 above and Algorithms 4, 5). In addition, we performed reconstruction using 100% of the data (without the addition of noise) via conventional MRF (Algorithm 1), for comparison purposes and to evaluate the error caused by the effect of a discretized dictionary. All the iterative algorithms were run until the difference between consecutive iterations was below the same threshold.

The MATLAB code for reproducing the experiment provided in this section can be found at: http://webee.techni-on.ac.il/Sites/People/YoninaEldar/software_det18.php. In this code, spiral sampling trajectories design was based on Lee et al.[60]

Figure 6 shows the resulting maps for the recovery of T1, T2, and PD obtained with the various algorithms against the reference (left). To allow detailed view of the reconstruction results, Fig. 6 shows a zoomed region for each map. Figure 7 shows the relative error maps with respect to the reference. To provide a scalar value of the error for each resulting map,

FIG. 5. One of the spiral trajectories use for undersampling a single image. Each time, the trajectories are rotated by 15 degrees. [Color figure can be viewed at wileyonlinelibrary.com]
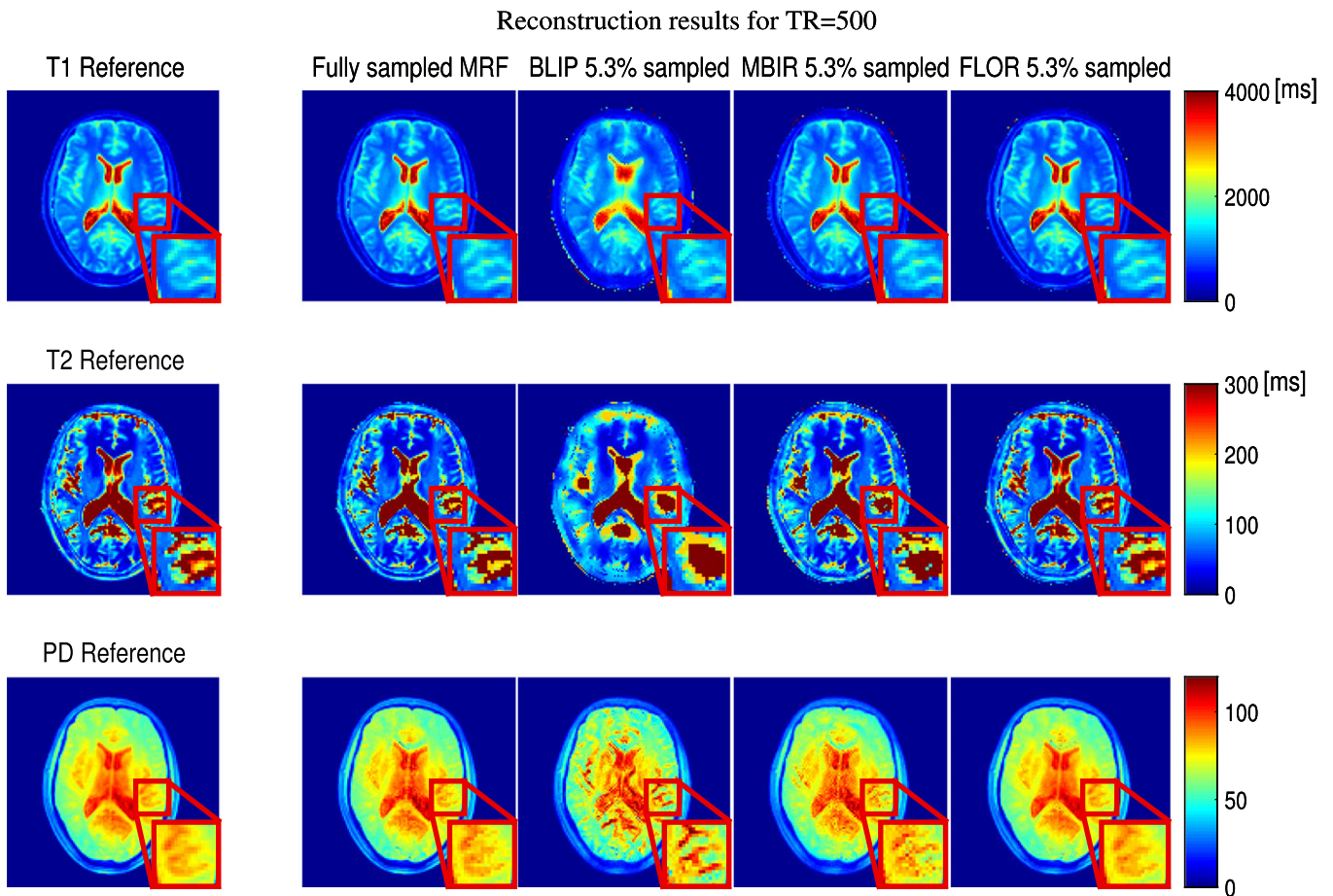

Reconstruction results for TR=500

FIG. 6. Reconstruction results of T1 and T2 in milliseconds, and PD in arbitrary units. Left: Reference maps, reconstruction using conventional MRF from 100% of the noise-free data, followed by BLIP, MBIR-MRF, and FLOR reconstruction with extension (as described in Section II.D) from 5% of the noisy data. [Color figure can be viewed at wileyonlinelibrary.com]
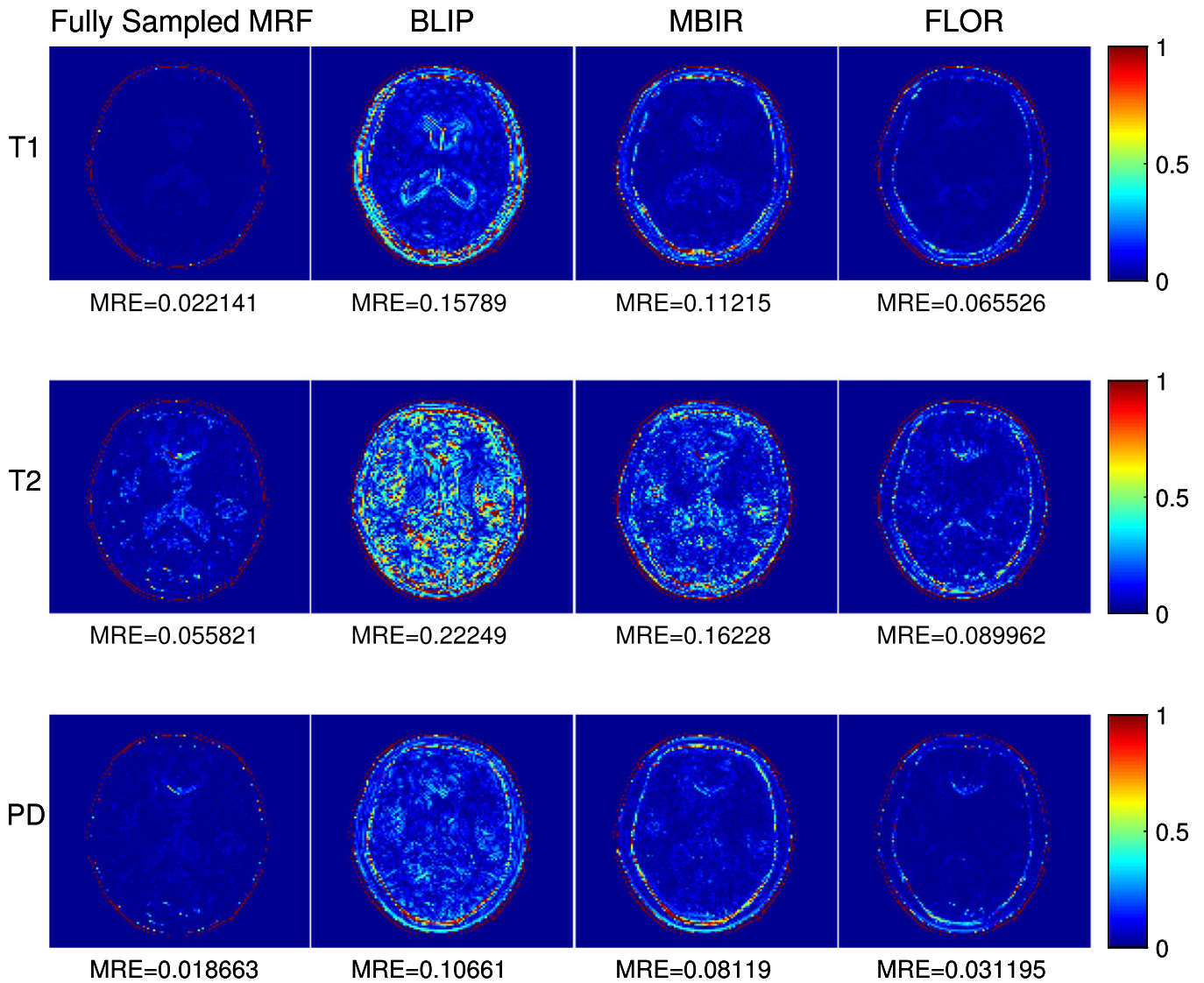
Relative error Maps for TR=500

FIG. 7. Relative error maps of the reconstruction of T1 and T2 in milliseconds, and PD in arbitrary units. Left: reconstruction using conventional MRF from 100% of the noise-free data, followed by BLIP, MBIR-MRF, and FLOR reconstruction with extension (as described in Section II.D) from 5% of the noisy data. [Color figure can be viewed at wileyonlinelibrary.com]

we calculated the mean relative error (MRE) between each quantitative map estimation and the reference map, defined as:

$$\mathrm{MRE}_i = \frac{1}{N} \sum_{j=1}^{N} \frac{|\theta_i^j - \hat{\theta}_i^j|}{\theta_i^j} \qquad (8)$$

where θ, $\hat{\theta}$ represent a reference map (such as T1,T2, or PD) and its corresponding reconstructed map (respectively), and j is a spatial index. In Appendix B we provide the results when TR = 300 and TR = 400 were used.

Note that the reference data in experiment 1 are the T1, T2, and PD maps resulting from DESPOT1 and DESPOT2. The fully sampled MRF results that appear in the leftmost column of Fig. 6 (with corresponding error maps in Fig. 7) were obtained by simulating the FISP sequence, fully

sampling the acquired data (instead of using undersampling via spiral trajectories), and then performing matching against the dictionary. Therefore, the fully sampled MRF results contain errors, which are mainly due to the fact that the dictionary is quantized.

It can be seen that both FLOR and MBIR-MRF outperform BLIP reconstruction results, when using 5% of sampled data by utilizing the low rank property. In addition, FLOR provides a lower error compared to MBIR-MRF. The details in the FLOR maps are comparable to those obtained by the original MRF algorithm using 100% of the noise-free data. Due to the very low sampling ratio in our experiments (measured as the number of samples divided by the number of pixels in the image), conventional MRF using 5% of the data
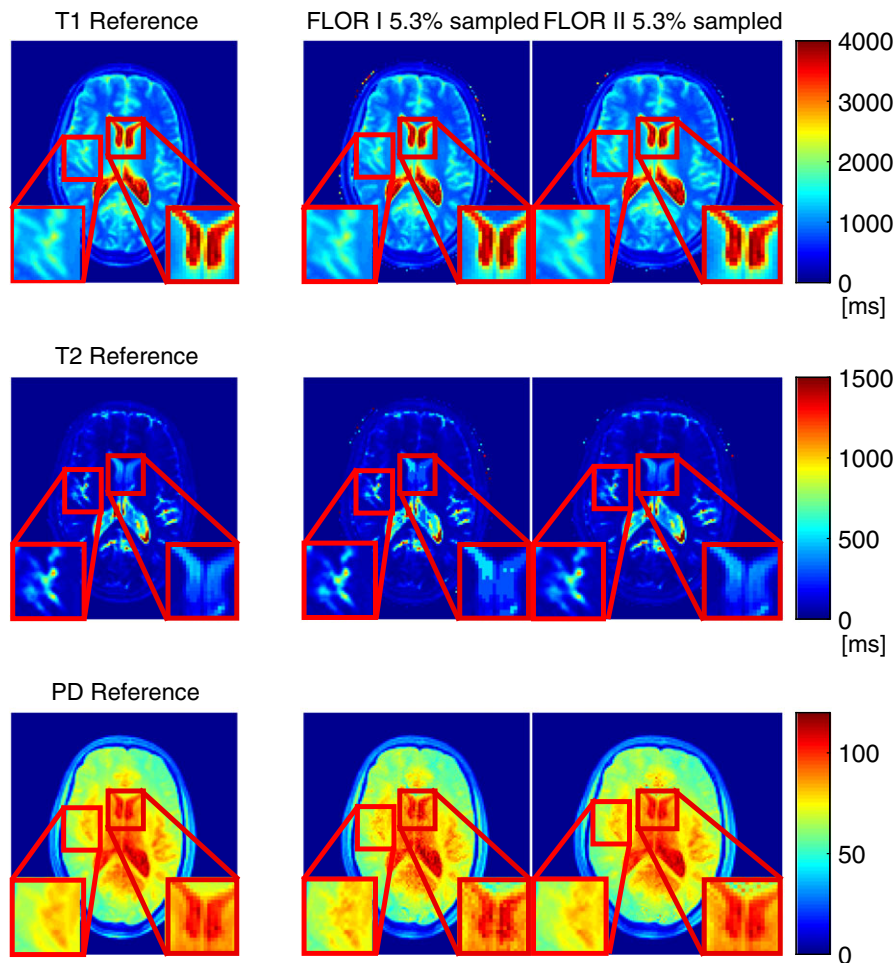
FIG. 8. Comparison of FLOR recovery with regular MF (FLOR I), and FLOR recovery with extension (FLOR II, as described in Section II.D) out of 5% of the data. T1 and T2 maps are in milliseconds, and PD is in arbitrary units. As can be seen in the magnified areas, FLOR II demonstrates a smoother solution (with less quantization errors) which is more similar to the original reference maps. [Color figure can be viewed at wileyonlinelibrary.com]

did not provide valuable reconstruction results and is therefore omitted in this analysis.

We next implemented the MF improvement described in Section II.D. The results are shown in Fig. 8, with corresponding relative error maps in Fig. 9. These figures compare the recovery maps of FLOR without (FLOR I) and with (FLOR II) the proposed improvement. It can be seen that FLOR II improves the results of FLOR I and produces a smoother solution which better fits the reference maps.

3.B. Experiment 2: *In vivo* prospective sampling experiment

The experiment in this section was carried out using the data of the original MRF paper,[19] which consisted of 48 spiral trajectories shifted by 7.5 degrees, where 1450 samples were acquired in each trajectory, leading to an underampling ratio of 9%. The data were acquired with IR-bSSFP pulse sequence and the pulses were amplitude modulated. The bSSFP sequence alternated their phase between 0 and 180 degrees to address the usual bSSFP banding artifacts. Data

was acquired on a 1.5-T whole body scanner (Espree, SIEMENS Healthcare) using a 32-channel head receiver coil. To handle multichannel acquisition, coil sensitivity maps were estimated from the data using the adaptive combine method.[61] In addition, the forward and adjoint spatial Fourier transforms ($F\{\cdot\}$ and $F^H\{\cdot\}$) were updated accordingly to support multichannel data using an extension of the NUFFT code developed by Chiew.[62]

Due to the lack of gold standard maps for this data, we are unable to provide quantitative error results (e.g., NMSE). Therefore, in this experiment, we compare between the various algorithms by examining reconstruction results using 400 TRs (representing 40% of scanning time) to quantitative values of brain tissues from the literature. Since the results obtained in the original MRF experiment (using 1000 TRs) mostly correspond to quantitative values from the literature, the maps generated using 1000 TRs using the original MRF algorithm are provided in Fig. 10, for reference. Those maps required acquisition time of 12.3 s for 1000 TRs, as reported in Ma et al.[19] In this experiment, we compare between the algorithms' results using 400 TRs (as using 1000 TRs leads to similar

Reference maps

Relative error maps

T1 Reference

T2 Reference

PD Reference

FLOR I

FLOR II

MRE=0.067893   MRE=0.065526

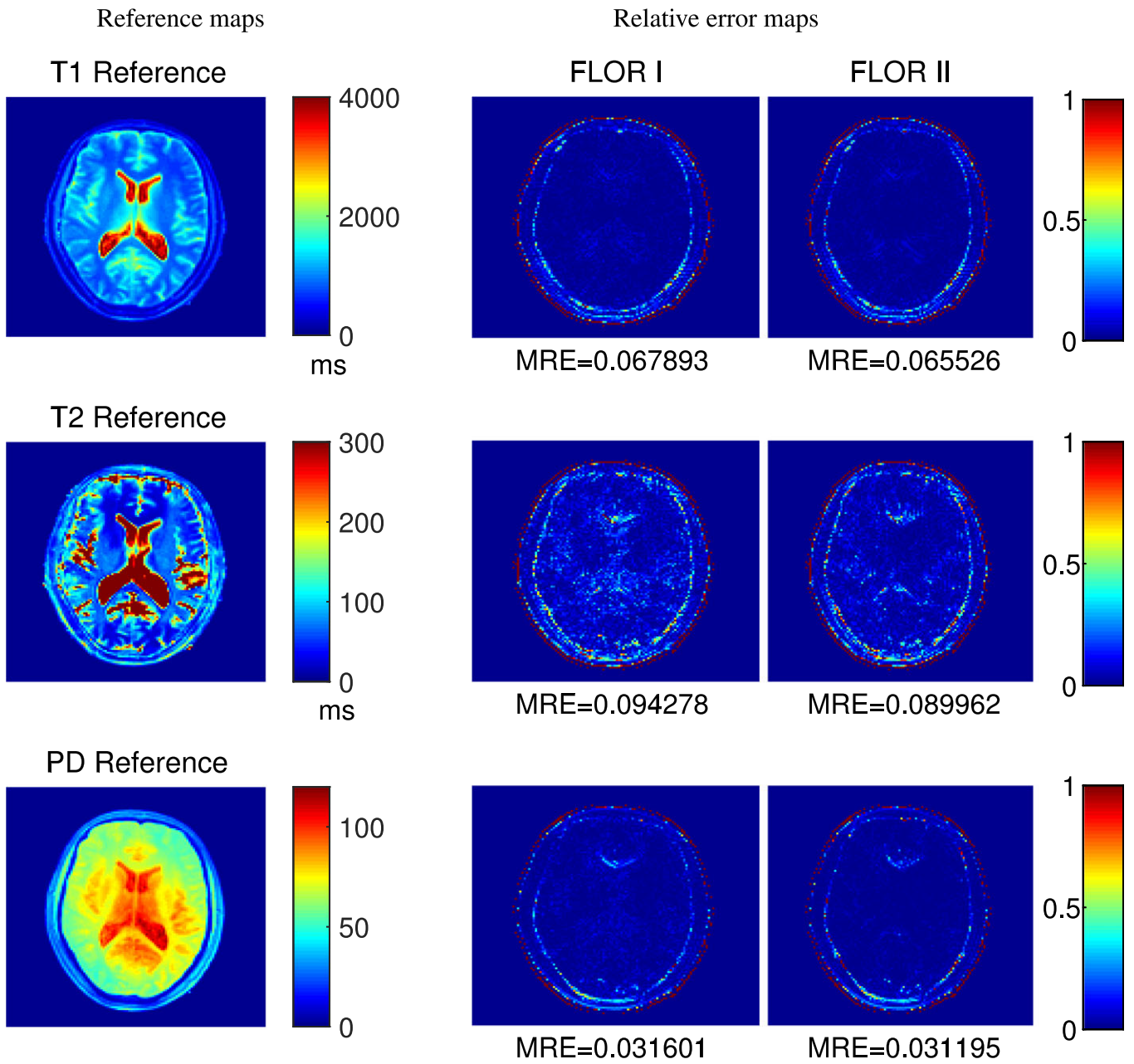MRE=0.094278   MRE=0.089962

MRE=0.031601   MRE=0.031195

FIG. 9. Reference maps (left) and relative error maps comparison, FLOR I vs FLOR II (right). It can be seen that FLOR II outperforms FLOR I. [Color figure can be viewed at wileyonlinelibrary.com]
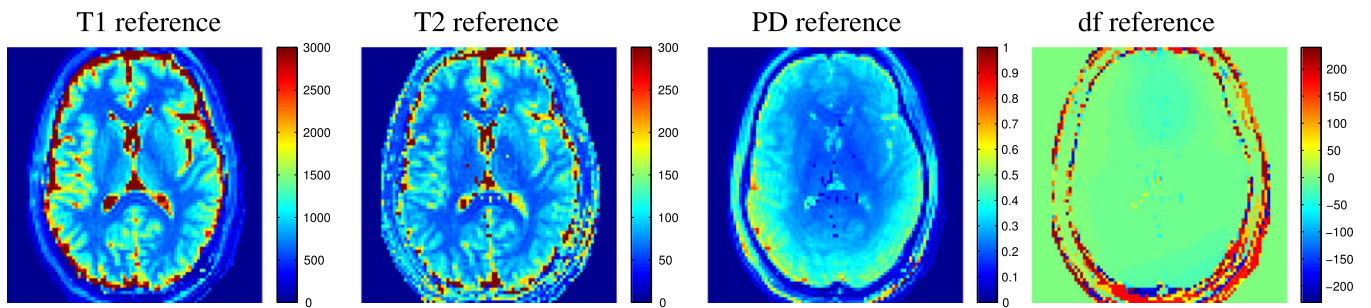
T1 reference   T2 reference   PD reference   df reference

FIG. 10. The maps obtained when applying the original MRF algorithm on 1000 TRs. T1 and T2 color scales are in milliseconds, and PD in normalized color scale and df color scale in Hz. [Color figure can be viewed at wileyonlinelibrary.com]

results for all methods), which is equivalent to a shortened acquisition time of 4.92 s.

The results of T1, T2, and PD maps for BLIP, MBIR-MRF, and FLOR appear in Fig. 12. Since IR-bSSFP sequence has been used in this experiment, off-resonance frequency has also been computed and shown. We used 109 different values in the range between −250 and 240 Hz. It can be seen that for T1, all iterative algorithms provide similar results, and T1 values of gray matter (GM), white matter (WM), and cerebrospinal fluid (CSF) regions correspond to similar values that appear in the literature (see Table I in Ma et al.[19]) and in Fig. 10. Noticeable artifacts appear in PD and T2 maps of all techniques. The artifacts are the result of using a shortened sequence (400 TRs instead of 1000 TRs in the original MRF paper). Since all the algorithms perform well for 1000 TRs, we shortened the sequence to show that low-rank/sparsity based methods can perform well, with a minimal rate of artifacts, also when using a shortened sequence. FLOR real data results for 1000 TRs can be seen in Fig. 11, showing T2 and PD maps with reduced artifacts.

While T2 results exhibit visible differences between the various methods, WM and GM values for all methods correspond to values that appear in the literature. However, both BLIP and MBIR MRF exhibit T2 values for CSF that are lower than those reported in the literature. Fig. 18 in Appendix C emphasizes this phenomenon, as it shows the same T2 results shown in Fig. 12, where the color scale for T2 is adjusted to 500–2000 ms (T2 values for CSF are around 2000 ms). Underestimation of T2 values in CSF regions was also reported in the original MRF experiment with 1000 TRs (and were justified as out-of-plane flow in this 2D experiment). In our case, using the same acquired data, it can be seen in Fig. 18 in Appendix C, that FLOR provides CSF values that better correspond to literature values, when compared to the other methods.

4. DISCUSSION

4.A. Relation to previous works

Although works that exploit the low-rank structure of MRF sequences have been published in the past,[32–35,37,40–42] our technique is unique mainly in the combination of convex

modeling and the ability to enable a solution with quantitative values that do not exist in the dictionary. Our solution is based on soft-thresholding the singular values,[52] which is mathematically justified in Appendix A.

Moreover, we compare our algorithm to both CS-based and low-rank based methods for MRF and demonstrate superior results. While BLIP treats the original MRF problem as an ℓ_0 optimization problem, FLOR first solves the relaxed problem of (6) and only then uses a MF to extract the magnetic parameters. It leads to some beneficial properties such as convergence guarantees, and the ability to use the acceleration step as described in Algorithm 4.

4.B. Computational complexity

FLOR is divided into two main components: The first recovers the imaging contrasts, and the second extracts the parameter maps from the recovered contrasts. The computational burden of FLOR lies in the low-rank projection step, or specifically, in the SVD calculation. This step does not exist in BLIP nor the original MRF reconstruction. However, there are efficient fast techniques to calculate the SVD,[63] required by FLOR. Note that the computation times reported in Table I were computed using the standard SVD approach implemented in MATLAB. Implementing an efficient technique for fast SVD is expected to significantly reduce FLOR computation times. Moreover, unlike BLIP, and other low rank based algorithms such as MBIR-MRF, FLOR does not require the pattern recognition calculation at every iteration. Another time consuming step that exists in all algorithms is the nonuniform Fourier transform. By using the acceleration step, FLOR reduces significantly the number of iterations required for convergence and therefore saves computational cost.

In addition, while previous implementations of CS-based reconstruction algorithms mainly use the inverse NUFFT (iNUFFT) algorithm, in our retrospective experiments we use SPURS.[64] Based on our observations, SPURS provides improved image reconstruction with the same computational complexity compared to iNUFFT. In the prospective sampling experiment, we used NUFFT and not SPURS because: (a) SPURS is still under development and currently does not support multichannel acquisition and; (b) to allow a fair comparison against the results of the original MRF algorithm,[19] that were also obtained using NUFFT.
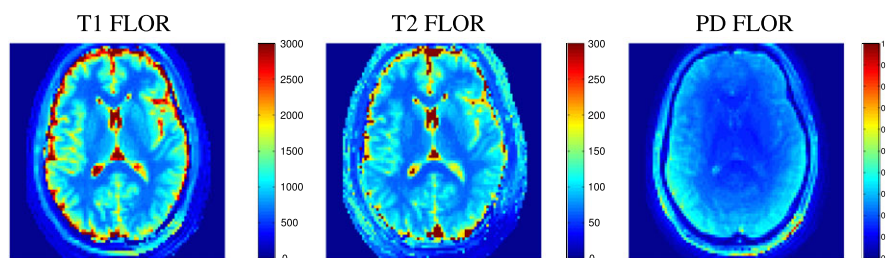

FIG. 11. The maps obtained when applying FLOR algorithm on 1000 TRs. T1 and T2 color scales are in milliseconds and PD in normalized color scale. Artifacts that appear in 400 TRs for T2 and PD maps are reduced. [Color figure can be viewed at wileyonlinelibrary.com]
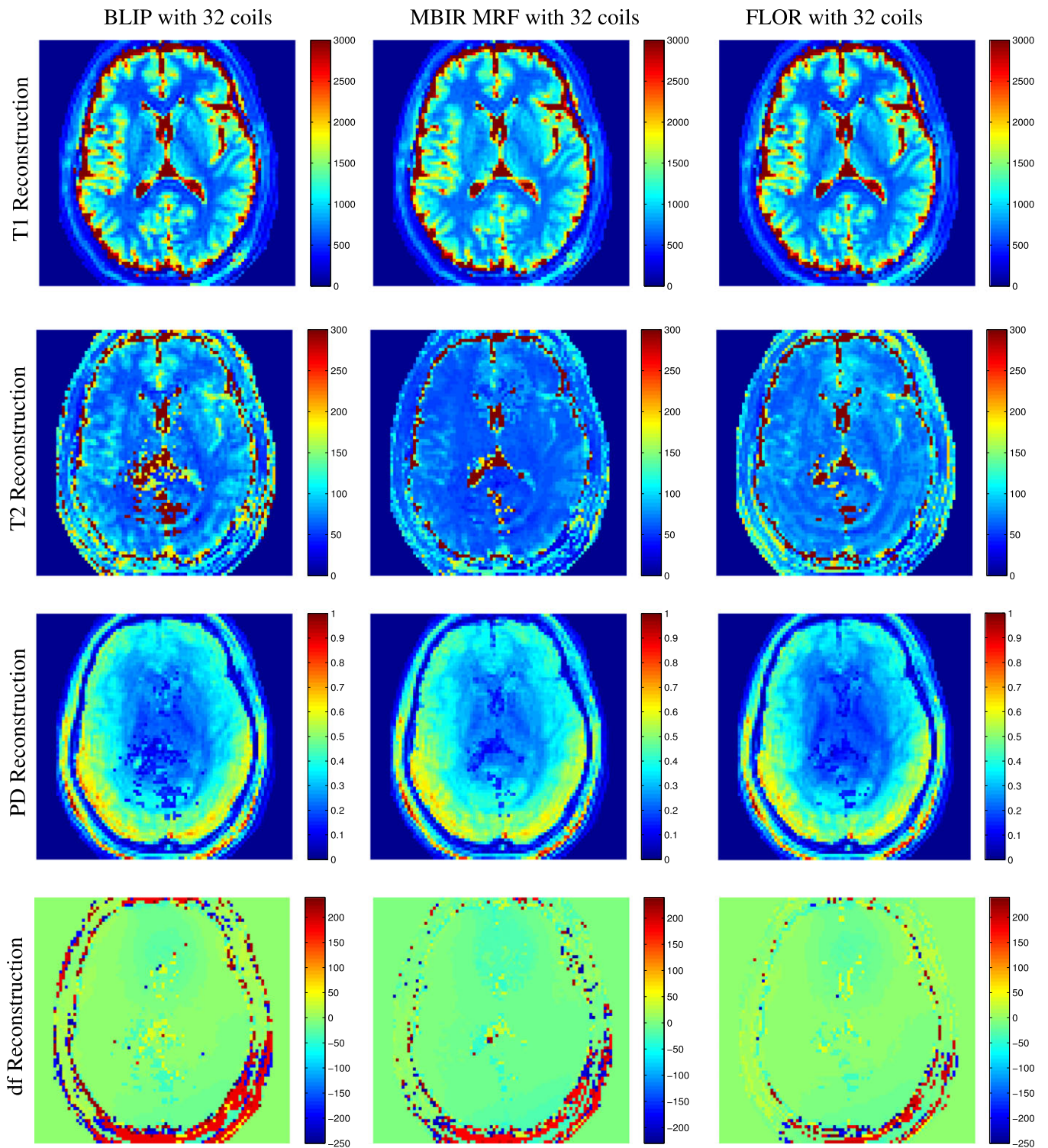
FIG. 12. Comparison between BLIP, MBIR-MRF, and FLOR reconstructions with data acquired out of 32 coils and 400 TRs. T1 and T2 color scales are in milliseconds, and PD in normalized color scale and df color scale in Hz. [Color figure can be viewed at wileyonlinelibrary.com]

5. CONCLUSIONS

We presented FLOR, a method for high quality reconstruction of quantitative MRI data using MRF, by utilizing the low-rank property of MRF data. Due to the fact that we exploit low-rank on top of the well known sparsity of MRF in the dictionary matching domain, we are able to obtain high quality reconstruction from highly undersampled data. Our method is based on a convex minimization problem, leading to a

solution in the dictionary subspace that overcomes its quantization error.

We provide results that are comparable to fully sampled MRF, using only 5% of the data in a simulation environment. In addition, comparison against CS-based and low-rank based methods for MRF shows the added value of our approach in generating quantitative maps with less artifacts. Our results consist of real-data, *in vivo* experiments that exhibit FLOR superiority also for realistic multicoil data acquisition. Future work will examine more sophisticated patch wise recoveries and additional experiments with different undersampling patterns.
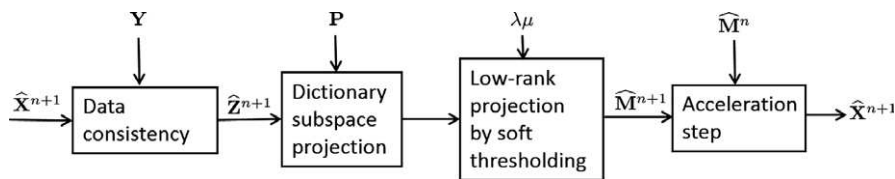
FIG. 13. A block diagram showing the main components of the core iterative stage of Algorithm 4. The final step in the diagram is the implementation of the acceleration step[55] for FLOR.
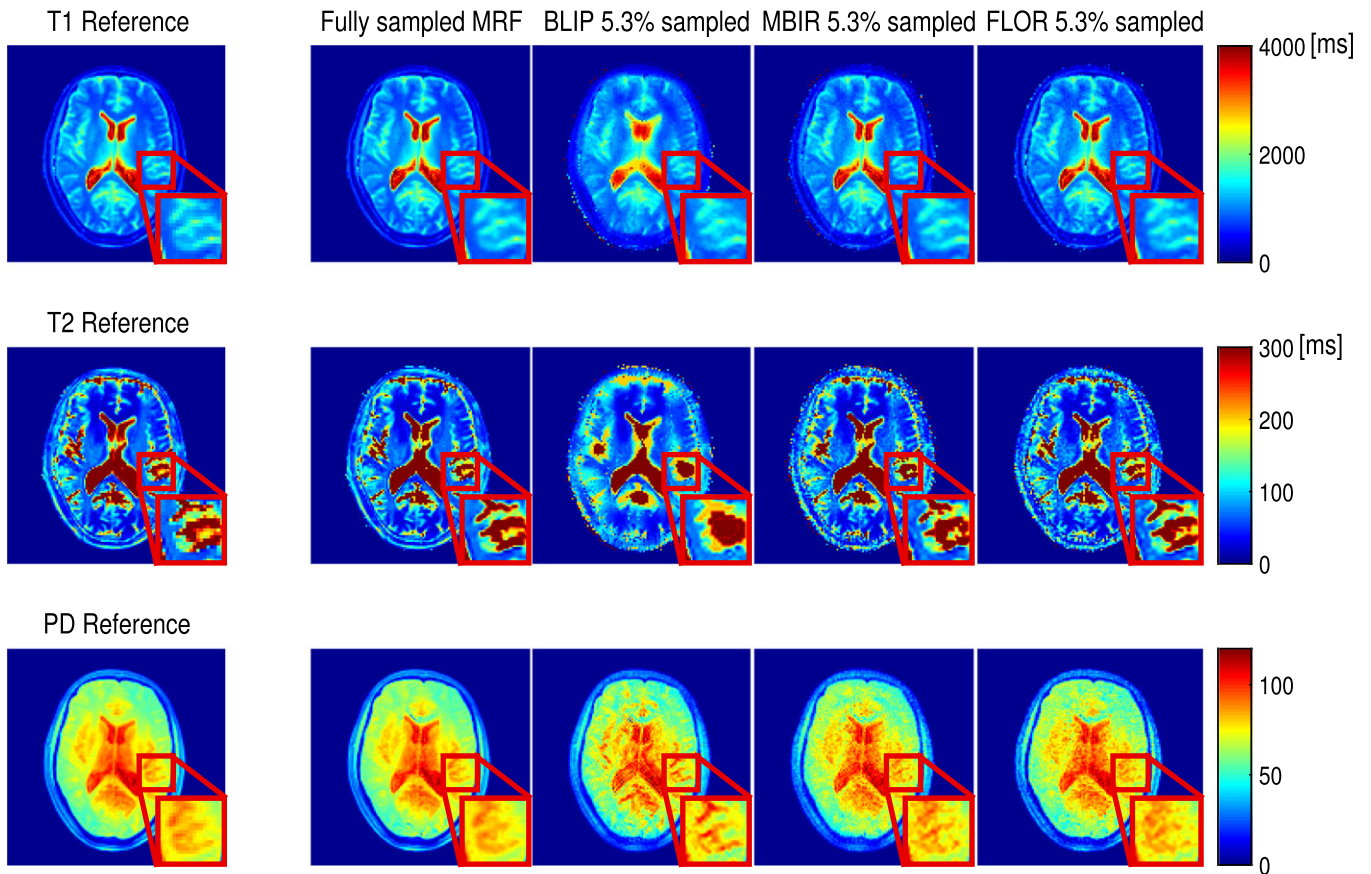

FIG. 14. Reconstruction results of T1 and T2 in milliseconds, and PD in arbitrary units, for TR = 300. Left: Reference maps, reconstruction using conventional MRF from 100% of the noise-free data, followed by BLIP, MBIR-MRF, and FLOR reconstruction with extension (as described in Section II.D) from 5% of the noisy data. [Color figure can be viewed at wileyonlinelibrary.com]

Relative error Maps for TR=300
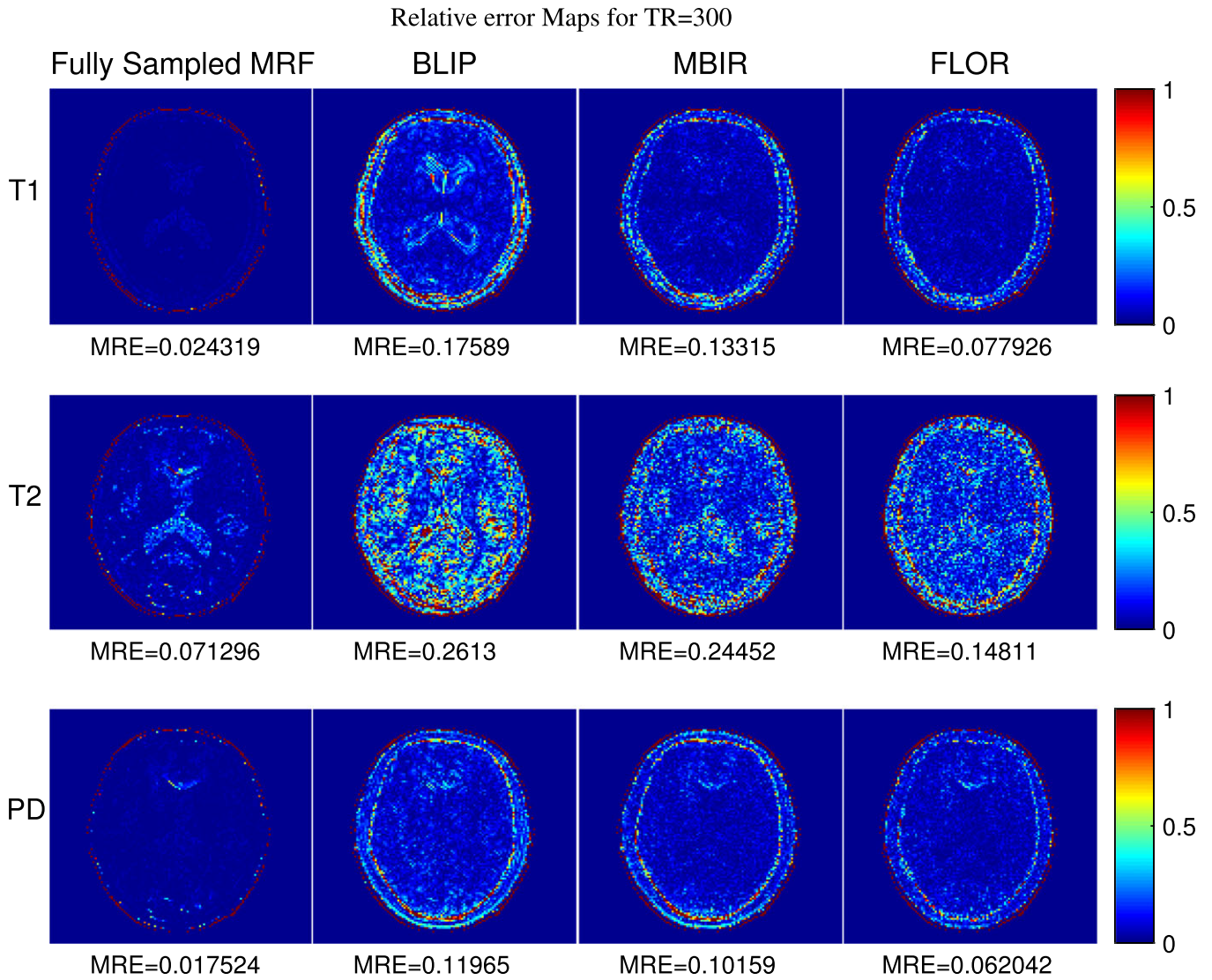
| Fully Sampled MRF | BLIP | MBIR | FLOR |

FIG. 15. Relative error maps of the reconstruction of T1 and T2 in milliseconds, and PD in arbitrary units. Left: reconstruction using conventional MRF from 100% of the noise-free data, followed by BLIP, MBIR-MRF, and FLOR reconstruction with extension (as described in Section II.D) from 5% of the noisy data. [Color figure can be viewed at wileyonlinelibrary.com]

APPENDIX A

The basic implementation of FLOR, as described in Algorithm 4 in the paper, aims to solve the following optimization problem:

$$\underset{\mathbf{X} \in \mathbb{D}}{\mathrm{argmin}} \frac{1}{2} \Sigma_i \left\| \mathbf{Y}_{:,i} - F_u \{ \mathbf{X}_{:,i} \} \right\|_2^2 + \lambda \| \mathbf{X} \|_* \qquad (A1)$$

where F_u is the partial Fourier transform operator, $\mathbf{X}$ has dimensions $N^2 \times L$ and $\mathbb{D} = \{ \mathbf{X} : \mathcal{N}(\mathbf{X}) \supseteq \mathcal{N}(\mathbf{D}) \}$.

FLOR solves (A1) using the incremental proximal method,[53] which treats problems of the form:

$$\underset{\mathbf{X} \in \mathbb{D}}{\mathrm{argmin}} \{ \Sigma_i^m F_i(\mathbf{X}) \} \qquad (A2)$$

where $F_i(\mathbf{X}) = f_i(\mathbf{X}) + h_i(\mathbf{X})$. The function $f_i(\mathbf{X})$ is convex and nondifferentiable, $h_i(\mathbf{X})$ is a convex function and $\mathbb{D}$ is a nonempty, closed, and convex subspace. The general step in solving (A2) is given by [27, (4.12)–(4.13)]:

$$\mathbf{Z}^k = P_{\mathbb{D}} (\mathbf{X}^k - \mu_k g_{i_k}) \qquad (A3a)$$

$$\mathbf{X}^{k+1} = \underset{\mathbf{X} \in \mathbb{D}}{\mathrm{argmin}} f_{i_k}(\mathbf{X}) + \frac{1}{2\mu_k} \| \mathbf{X} - \mathbf{Z}^k \|_F^2 \qquad (A3b)$$

where $g_{i_k} \in \partial h_{i_k}(\mathbf{X}^k)$, μ_k is a positive step size, and $P_{\mathbb{D}}$ is the projection operator onto $\mathbb{D}$ defined as
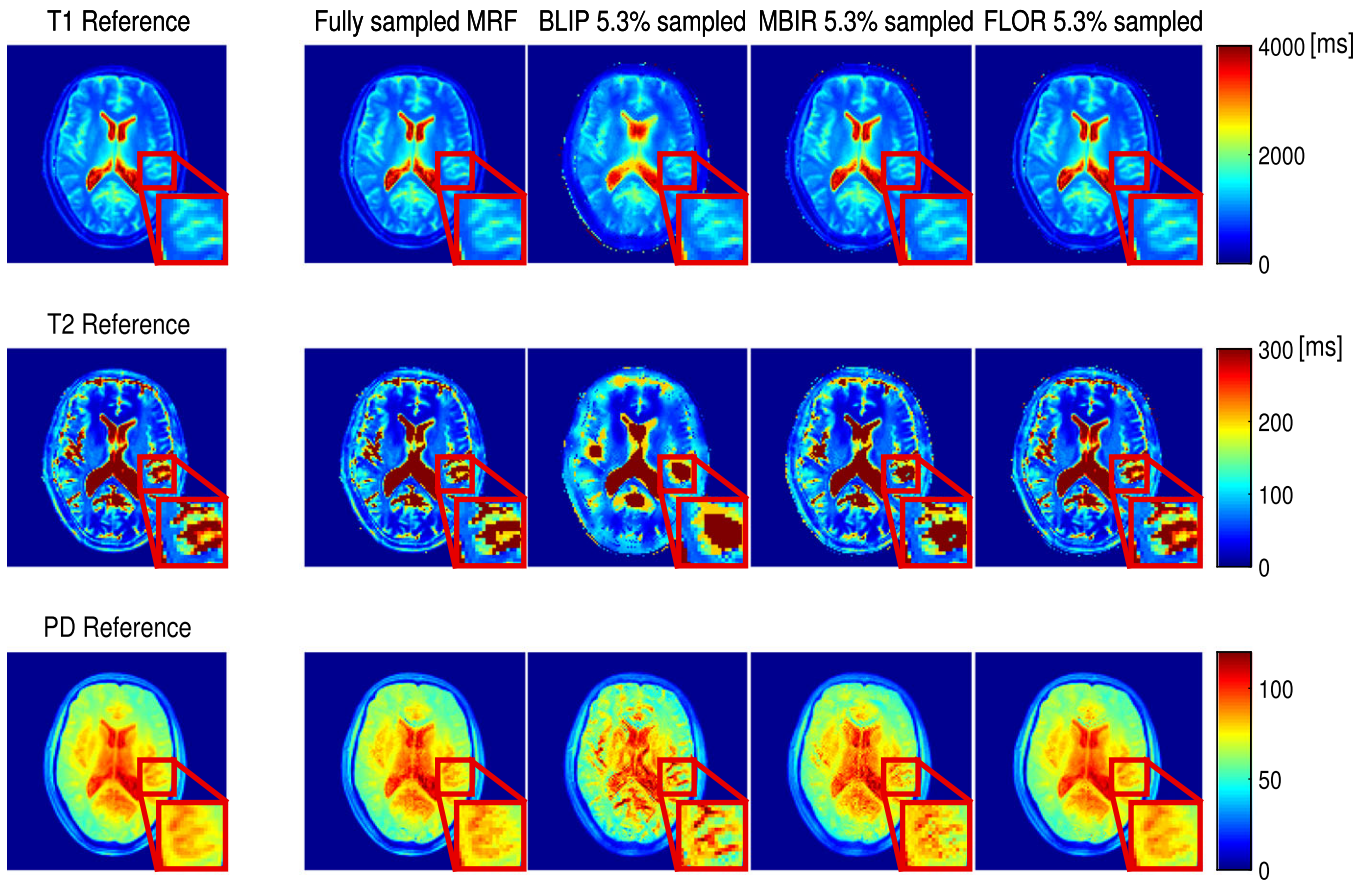
Reconstruction results for TR=400

FIG. 16. Reconstruction results of T1 and T2 in milliseconds, and PD in arbitrary units, for TR = 400. Left: Reference maps, reconstruction using conventional MRF from 100% of the noise-free data, followed by BLIP, MBIR-MRF, and FLOR reconstruction with extension (as described in Section II.D) from 5% of the noisy data. [Color figure can be viewed at wileyonlinelibrary.com]

$$P_{\mathbb{D}}(\mathbf{X}) = \operatorname*{argmin}_{\mathbf{Z} \in \mathbb{D}} \|\mathbf{Z} - \mathbf{X}\|_F^2. \tag{A4}$$

The optimization problem, defined in the update step of $\mathbf{X}^{k+1}$, is referred to as the proximal gradient calculation of the nondifferentiable f_{i_k}, under the constraint $\mathbf{X} \in \mathbb{D}$.

Our problem in Eq. (A1) corresponds to $m = 1$ in Eq. (A2) and

$$h(\mathbf{X}) = \frac{1}{2}\sum_i \left\|\mathbf{Y}_{:,i} - F_u\{\mathbf{X}_{:,i}\}\right\|_2^2 = \frac{1}{2}\|\mathbf{Y} - F_u\{\mathbf{X}\}\|_F^2$$

$$f(\mathbf{X}) = \lambda\|\mathbf{X}\|_*. \tag{A5}$$

Therefore,

$$\partial h(\mathbf{X}) = F_u^H\{\mathbf{Y} - F_u\{\mathbf{X}\}\}, \tag{A6}$$

and

$$P_{\mathbb{D}}(\mathbf{X}) = \mathbf{X}\mathbf{D}^\dagger\mathbf{D} = \mathbf{X}\mathbf{P}. \tag{A7}$$

The solution of (A3b) for $f(\mathbf{X}) = \lambda\|\mathbf{X}\|_*$ without the constraint $\mathbf{X} \in \mathbb{D}$ is the singular value soft-thresholding operator (SVT)[52] defined as:

$$\operatorname{SVT}_{\mu_k\lambda}(\mathbf{Z}^k) = \mathbf{U}_r[\mathbf{\Sigma}_r - \mu_k\lambda\mathbf{I}]_+\mathbf{V}_r^H. \tag{A8}$$

Here, $\mathbf{\Sigma}_r$ is a diagonal matrix with the non-zero singular values of $\mathbf{Z}^k$ on its diagonal, $\mathbf{U}_r$ and $\mathbf{V}_r$ are the r left and right singular vectors of the SVD of $\mathbf{Z}^k$, associated with the r non-zero singular values, and $[x]_+ = \max(0,x)$. In our case, since $\mathbf{Z}^k \in \mathbb{D}$ (as follows from (A3a)) and the SVT calculation keeps the operand in the same subspace, the constraint $\mathbf{X} \in \mathbb{D}$ can be omitted. Therefore, (A3b) reduces to

$$\mathbf{X}^{k+1} = \mathbf{U}_r[\mathbf{\Sigma}_r - \mu_k\lambda\mathbf{I}]_+\mathbf{V}_r^H. \tag{A9}$$

Combining (A6), (A9), and (A7), the incremental subgradient-proximal method for solving (A1) consists of two updates in each iteration:

$$\mathbf{Z}^k = (\mathbf{X}^k - \mu_k F_u^H\{\mathbf{Y} - F_u\{\mathbf{X}^k\}\})\mathbf{P} \tag{A10a}$$

$$\mathbf{X}^{k+1} = \mathbf{U}_r[\mathbf{\Sigma}_r - \mu_k\lambda\mathbf{I}]_+\mathbf{V}_r^H. \tag{A10b}$$

This constitutes the core of Algorithm 4. In our framework, the step sizes are set to constant, $\mu_k = \mu$, and λ is chosen experimentally.

Figure 13 shows a block diagram of the iterations of Algorithm 4, after implementing the acceleration step.[55]
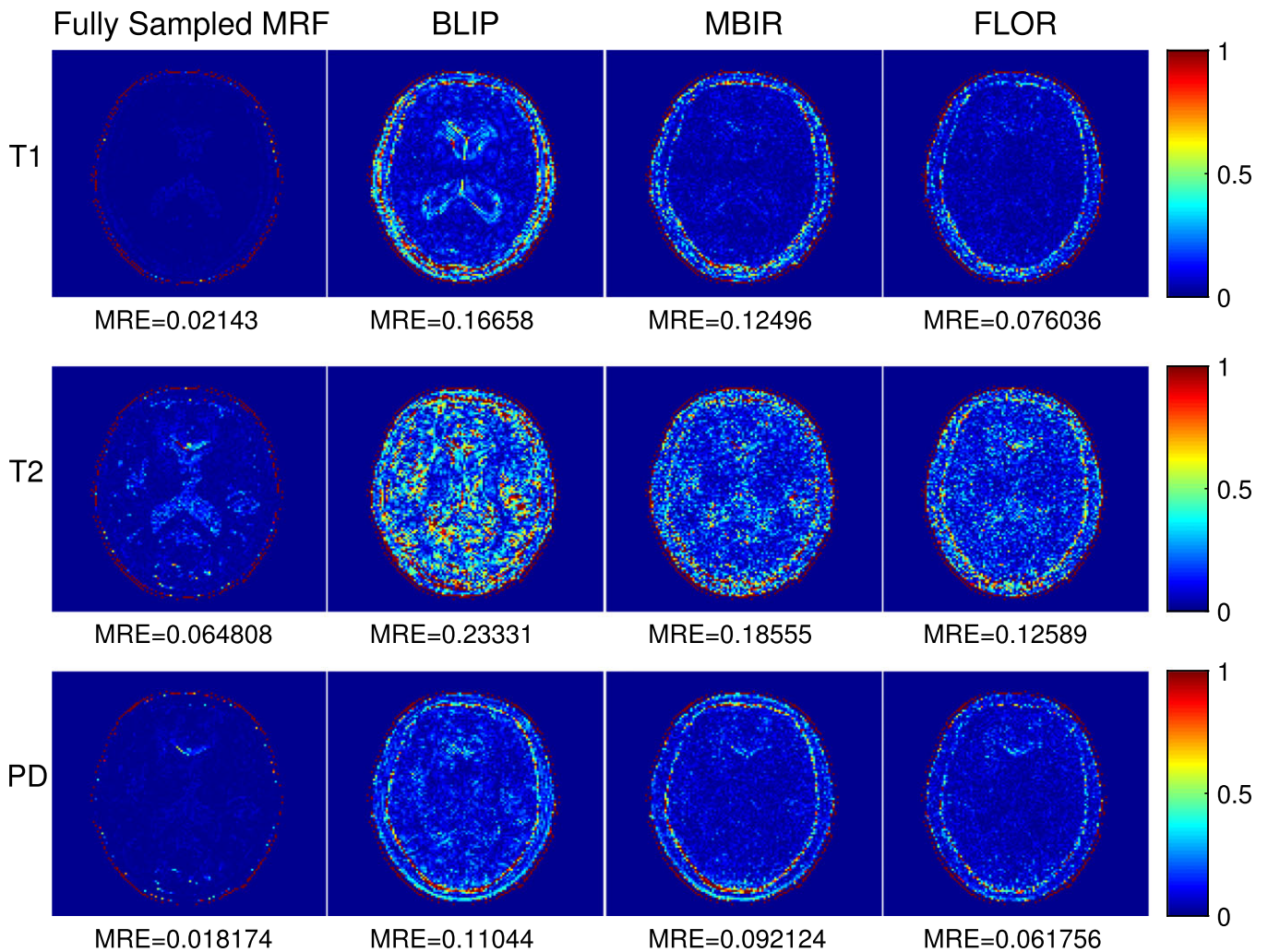
Relative error Maps for TR=400

FIG. 17. Relative error maps of the reconstruction of T1 and T2 in milliseconds, and PD in arbitrary units. Left: reconstruction using conventional MRF from 100% of the noise-free data, followed by BLIP, MBIR-MRF, and FLOR reconstruction with extension (as described in Section II.D) from 5% of the noisy data. [Color figure can be viewed at wileyonlinelibrary.com]
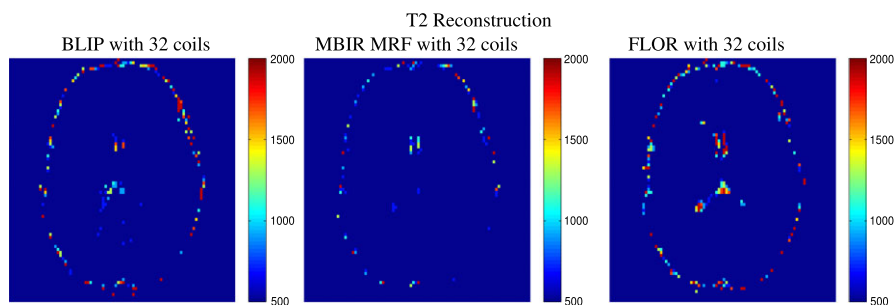

FIG. 18. Comparison between T2 map reconstructions of BLIP, MBIR-MRF and FLOR with sequence length of 400 TRs. T2 color scales are above 500 ms. It can be seen that FLOR provides T2 values for CSF that better match the literature values in this case. [Color figure can be viewed at wileyonlinelibrary.com]

APPENDIX B

In this Appendix, we present the results of all the methods for TR = 300 and TR = 400. Figures 14 and 15 show the parameter and error maps for TR = 300, and Figs. 16 and 17 show the parameter and error maps for TR = 400. By examining the results shown in this Appendix, as well as the results for TR = 500 (in Figs. 6 and 7), it can clearly be seen that increasing the number of TRs improves the performance

of all approaches, while in all cases MBIR outperforms BLIP, and FLOR is the most reliable one.

APPENDIX C

In this Appendix, we present in Fig. 18 the same T2 maps shown in Fig. 12, where the color scale is adjusted to 500–2000 ms (T2 values for CSF are around 2000 ms). Using the same acquired data, it can be seen that FLOR provides CSF values that better correspond to literature values, when compared to the other methods.

a)Author to whom correspondence should be addressed. Electronic mail: galmazor@campus.technion.ac.il; Telephone: +972-7-78871725.

REFERENCES

1. Ehses P, Seiberlich N, Ma D, et al. IR TrueFISP with a golden-ratio-based radial readout: fast quantification of T1, T2, and proton density. *Magn Reson Med*. 2013;69:71–81.
2. Baselice F, Ferraioli G, Pascazio V. A Bayesian approach for relaxation times estimation in MRI. *Magn Reson Imaging*. 2016;34: 312–325.
3. Antonini A, Leenders KL, Meier D, Oertel WH, Boesiger P, Anliker M. T2 relaxation time in patients with Parkinson's disease. *Neurology*. 1993;43:697–697.
4. Baselice F, Ferraioli G, Grassia A, Pascazio V. Optimal configuration for relaxation times estimation in complex spin echo imaging. *Sensors*. 2014;14:2182–2198.
5. Haley AP, Knight-Scott J, Fuchs KL, Simnad VI, Manning CA. Shortening of hippocampal spin-spin relaxation time in probable Alzheimer's disease: a 1 h magnetic resonance spectroscopy study. *Neurosci Lett*. 2004;362:167–170.
6. Mariappan SV, Subramanian S, Chandrakumar N, Rajalakshmi KR, Sukumaran SS. Proton relaxation times in cancer diagnosis. *Magn Reson Med*. 1988;8:119–128.
7. Roebuck JR, Haker SJ, Mitsouras D, Rybicki FJ, Tempany CM, Mulkern RV. Carr-Purcell-Meiboom-Gill imaging of prostate cancer: quantitative T2 values for cancer discrimination. *Magn Reson Imaging*. 2009;27:497–502.
8. Liu J, Nieminen AO, Koenig JL. Calculation of T1, T2, and proton spin density images in nuclear magnetic resonance imaging. *J Magn Reson (1969)*. 1989;85:95–110.
9. Homer J, Beevers MS. Driven-equilibrium single-pulse observation of T1 relaxation. A reevaluation of a rapid new method for determining NMR spin-lattice relaxation times. *J Magn Reson (1969)*. 1985;63:287–297.
10. Crooijmans HJA, Scheffler K, Bieri O. Finite RF pulse correction on DESPOT2. *Magn Reson Med*. 2011;65:858-862.
11. Yarnykh VL. Actual flip-angle imaging in the pulsed steady state: a method for rapid three-dimensional mapping of the transmitted radiofrequency field. *Magn Reson Med*. 2007;57:192–200.
12. Hurley SA, Yarnykh VL, Johnson KM, Field AS, Alexander AL, Samsonov AA. Simultaneous variable flip angle-actual flip angle imaging method for improved accuracy and precision of three-dimensional t1 and b1 measurements. *Magn Reson Med*. 2012; 68:54–64.
13. Schmitt P, Griswold MA, Jakob PM, et al. Inversion recovery TrueFISP: quantification of T1, T2, and spin density. *Magn Reson Med*. 2004;51:661–667.
14. Doneva M, Börnert P, Eggers H, Stehning C, Sénégas J, Mertins A. Compressed sensing reconstruction for magnetic resonance parameter mapping. *Magn Reson Med*. 2010;64:1114–1120.
15. Zhao B, Lu W, Hitchens TK, Lam F, Ho C, Liang Z-P. Accelerated MR parameter mapping with low-rank and sparsity constraints. *Magn Reson Med*. 2015;74:489–498.
16. Petzschner FH, Ponce IP, Blaimer M, Jakob PM, Breuer FA. Fast MR parameter mapping using k-t principal component analysis. *Magn Reson Med*. 2011;66:706–716.
17. Huang C, Graff CG, Clarkson EW, Bilgin A, Altbach MI. T2 mapping from highly undersampled data by reconstruction of principal component coefficient maps using compressed sensing. *Magn Reson Med*. 2012;67:1355–1366.
18. Velikina JV, Alexander AL, Samsonov A. Accelerating MR parameter mapping using sparsity-promoting regularization in parametric dimension. *Magn Reson Med*. 2013;70:1263–1273.
19. Ma D, Gulani V, Seiberlich N, et al. Magnetic resonance fingerprinting. *Nature*. 2013;495:187–192.
20. Fessler JA, Sutton BP. Nonuniform fast fourier transforms using min-max interpolation. *IEEE Trans Sign Process*. 2003;51:560–574.
21. Jiang Y, Ma D, Seiberlich N, Gulani V, Griswold MA. MR fingerprinting using fast imaging with steady state precession (FISP) with spiral readout. *Magn Reson Med*. 2015;74:1621–1631.
22. Eldar YC, Kutyniok G. *Compressed Sensing: Theory and Applications*. Cambridge: Cambridge University Press; 2012.
23. Eldar YC. *Sampling Theory: Beyond Bandlimited Systems*. Cambridge: Cambridge University Press; 2015.
24. Davies M, Puy G, Vandergheynst P, Wiaux Y. A compressed sensing framework for magnetic resonance fingerprinting. *SIAM J Imaging Sci*. 2014;7:2623–2656.
25. Wang Z, Li H, Zhang Q, Yuan J, Wang X. Magnetic resonance fingerprinting with compressed sensing and distance metric learning. *Neurocomputing*. 2016;174:560–570.
26. Zhao B, Setsompop K, Ye H, Cauley SF, Wald LL. Maximum likelihood reconstruction for magnetic resonance fingerprinting. *IEEE Trans Med Imaging*. 2016;35:1812–1823.
27. Lingala SG, Hu Y, DiBella E, Jacob M. Accelerated dynamic MRI exploiting sparsity and low-rank structure: k-t SLR. *IEEE Trans Med Imaging*. 2011;30:1042–1054.
28. Zhao B, Haldar JP, Christodoulou AG, Liang Z-P. Image reconstruction from highly undersampled (k, t)-space data with joint partial separability and sparsity constraints. *IEEE Trans Med Imaging*. 2012;31:1809–1820.
29. Zhao B, Haldar JP, Brinegar C, Liang Z-P. Low rank matrix recovery for real-time cardiac MRI. In: *Biomedical Imaging: From Nano to Macro, 2010 IEEE International Symposium on*. IEEE; 2010:996–999.
30. Feng L, Srichai MB, Lim RP, et al. Highly accelerated real-time cardiac cine MRI using k-t sparse-sense. *Magn Reson Med*. 2013;70:64–74.
31. Chiew M, Smith SM, Koopmans PJ, Graedel NN, Blumensath T, Miller KL. k-t faster: acceleration of functional MRI data acquisition using low rank constraints. *Magn Reson Med*. 2015;74:353–364.
32. McGivney DF, Pierre E, Ma D, et al. SVD compression for magnetic resonance fingerprinting in the time domain. *IEEE Trans Med Imaging*. 2014;33:2311–2322.
33. Cline CC, Chen X, Mailhe B, Wang Q, Nadar M. Model-based iterative reconstruction for magnetic resonance fingerprinting. In: *Proceedings of the International Society of Magnetic Resonance in Medicine (ISMRM)*; 2016:434.
34. Zhao B. Model-based iterative reconstruction for magnetic resonance fingerprinting. In: *Image Processing (ICIP), 2015 IEEE International Conference on*. IEEE; 2015:3392–3396.
35. Zhao B, Setsompop K, Gagoski B, et al. A model-based approach to accelerated magnetic resonance fingerprinting time series reconstruction. In: *Proceedings of the International Society of Magnetic Resonance in Medicine (ISMRM)*; 2016:871.
36. Mazor G, Weizman L, Eldar YC, Tal A. Low rank magnetic resonance fingerprinting. In: *Proceedings of the 38th international conference of the IEEE Engineering in Medicine and Biology (EMBC)*. IEEE; 2016:439–442.
37. Liao C, Cao XC, Ye H, Chen Y, et al. Acceleration of mr fingerprinting with low rank and sparsity constraint. In: *Proceedings of the International Society of Magnetic Resonance in Medicine (ISMRM)*; 2016:4227.
38. Candès EJ, Li X, Ma Y, Wright J. Robust principal component analysis? *JACM*. 2011;58:11.
39. Doneva M, Amthor T, Koken P, Sommer K, Börnert P. Low-rank matrix completion-based reconstruction for undersampled magnetic resonance fingerprinting. In: *Proceedings of the International Society of Magnetic Resonance in Medicine (ISMRM)*; 2016:432.

40. Doneva M, Amthor T, Koken P, Sommer K, Börnert P. Matrix completion-based reconstruction for under-sampled magnetic resonance fingerprinting data. *Magn Reson Imaging*. 2017;41:41–52.

41. Zhao B, Setsompop K, Adalsteinsson E, et al. Improved magnetic resonance fingerprinting reconstruction with low-rank and subspace modeling. *Magn Reson Med*. 2018;79(2):933–942.

42. Assländer J, Cloos MA, Knoll F, Sodickson DK, Hennig J, Lattanzi R. Low rank alternating direction method of multipliers reconstruction for MR fingerprinting. *Magn Reson Med*. 2018;79:83–96.

43. Nedic A, Bertsekas DP. Incremental subgradient methods for nondifferentiable optimization. *SIAM J Optim*. 2001;12:109–138.

44. Lustig M, Donoho DL, Santos JM, Pauly JM. Compressed sensing MRI. *IEEE Sign Process Mag*. 2008;25:72–82.

45. Weizman L, Eldar YC, Bashat DB. Compressed sensing for longitudinal MRI: an adaptive-weighted approach. *Med Phys*. 2015;42:5195-5208.

46. Weizman L, Eldar YC, Bashat DB. Reference-based MRI. *Med Phys*. 2016;43:5357–5369.

47. Otazo R, Candes E, Sodickson DK. Low-rank plus sparse matrix decomposition for accelerated dynamic MRI with separation of background and dynamic components. *Magn Reson Med*. 2015;73:1125–1136.

48. Weizman L, Miller K, Eldar YC, Chiew M. PEAR: periodic and fixed rank separation for fast fMRI. *Med Phys*. 2018;44:6166–6182.

49. Deoni SCL, Peters TM, Rutt BK. High-resolution T1 and T2 mapping of the brain in a clinically acceptable time with DESPOT1 and DESPOT2. *Magn Reson Med*. 2005;53:237–241.

50. Hargreavs B. http://web.stanford.edu/ #˜bah/software/epg/.

51. Boyd S, Parikh N, Chu E, Peleato B, Eckstein J. Distributed optimization and statistical learning via the alternating direction method of multipliers. *Found Trends® Mach Learn*. 2011;3:1–122.

52. Cai J-F, Candès EJ, Shen Z. A singular value thresholding algorithm for matrix completion. *SIAM J Optim*. 2010;20:1956–1982.

53. Sra S, Nowozin S, Wright SJ. *Optimization for Machine Learning*. Cambridge, MA: MIT Press; 2012.

54. Nesterov Y. A method of solving a convex programming problem with convergence rate o (1/k2). In: *Soviet Mathematics Doklady*, Vol. 27; 1983:372–376.

55. Beck A, Teboulle M. A fast iterative shrinkage-thresholding algorithm for linear inverse problems. *SIAM J Imaging Sci*. 2009;2:183–202.

56. Palomar DP, Eldar YC. *Convex Optimization in Signal Processing and Communications*. Cambridge: Cambridge University Press; 2010.

57. Kiperwas A, Rosenfeld D, Eldar YC. The SPURS algorithm for resampling an irregularly sampled signal onto a cartesian grid. *IEEE Trans Med Imaging*. 2017;36:628–640.

58. Liberman G, Louzoun Y, Bashat DB. T1 mapping using variable flip angle SPGR data with flip angle correction. *J Magn Reson Imaging*. 2014;40:171–180.

59. Vymazal J, Righini A, Brooks RA, et al. T1 and T2 in the brain of healthy subjects, patients with parkinson disease, and patients with multiple system atrophy: relation to iron content 1. *Radiology*. 1999;211:489–495.

60. Lee JH, Hargreaves BA, Hu BS, Nishimura DG. Fast 3D imaging using variable-density spiral trajectories with applications to limb perfusion. *Magn Reson Med*. 2003;50:1276–1285.

61. Walsh DO, Gmitro AF, Marcellin MW. Adaptive reconstruction of phased array mr imagery. *Magn Reson Med*. 2000;43:682–690.

62. Chiew M. https://users.fmrib.ox.ac.uk/˜mchiew/research/.

63. Drmac Z, Veselic K. New fast and accurate Jacobi SVD algorithm: I. lapack working note 169; 2005.

64. Kiperwas A, Rosenfeld D, Eldar YC.. The SPURS algorithm for resampling an irregularly sampled signal onto a cartesian grid. *IEEE Trans Med Imaging*. 2017;36:628–640.